

# Distribution Learning for Molecular Regression

Nima Shoghi<sup>\*1</sup> Pooya Shoghi Anuroop Sriram<sup>2</sup> Abhishek Das<sup>\*</sup>

<sup>1</sup>Georgia Institute of Technology

<sup>2</sup>Fundamental AI Research (FAIR) at Meta

<sup>\*</sup>Work done while at FAIR

Correspondence to: [nimash@gatech.edu](mailto:nimash@gatech.edu)

July 31, 2024

## Abstract

Using “soft” targets to improve model performance has been shown to be effective in classification settings, but the usage of soft targets for regression is a much less studied topic in machine learning. The existing literature on the usage of soft targets for regression fails to properly assess the method’s limitations, and empirical evaluation is quite limited. In this work, we assess the strengths and drawbacks of existing methods when applied to molecular property regression tasks. Our assessment outlines key biases present in existing methods and proposes methods to address them, evaluated through careful ablation studies. We leverage these insights to propose Distributional Mixture of Experts (DMoE): A model-independent, and data-independent method for regression which trains a model to predict probability distributions of its targets. Our proposed loss function combines the cross entropy between predicted and target distributions and the L1 distance between their expected values to produce a loss function that is robust to the outlined biases. We evaluate the performance of DMoE on different molecular property prediction datasets – Open Catalyst (OC20), MD17, and QM9 – across different backbone model architectures – SchNet, GemNet, and Graphormer. Our results demonstrate that the proposed method is a promising alternative to classical regression for molecular property prediction tasks, showing improvements over baselines on all datasets and architectures.

## 1 Introduction

Graph Neural Networks (GNNs) have been shown to be quite successful at molecular property prediction [7, 12, 23, 9]. In these methods, systems are typically represented as graphs with atoms as nodes, and properties of interest as graph-level (e.g. energy) or node-level (e.g. atomic force) targets.

Orthogonal to the underlying GNN architecture, there is an abundance of methods that have been proposed to improve model generalization. Data augmentation methods – e.g. by adding Gaussian noise to atomic positions [13] – modify the input dataset to increase diversity and make the GNN robust to transformations without additional annotated data. Jointly training the GNN on auxiliary tasks (in addition to the main task of interest) – e.g., by adding an auxiliary position denoising loss [13] – has been shown to lead to better representations. Regularization techniques – e.g., penalizing overconfident predictions [19], randomly dropping nodes [6] and edges [21] in the input graph, and normalization layers [3, 32, 17, 33] – add further constraints to improve generalization.

We focus on a parallel set of techniques that change the target representations. In classification tasks, label smoothing [28] is one such technique that modifies the target distribution to be a mixture of categorical (i.e. one-hot) and uniform. In regression tasks –

which are more common for molecular prediction – Imani and White [15] proposed histogram regression, where the target scalars are converted to ‘soft’ probability distributions, and the model is trained to predict these distributions.

In this paper, we begin by conducting a thorough analysis of Imani and White [15]’s histogram regression and find that it is not well-suited for molecular property prediction tasks. We identify key biases in histogram regression and propose strategies to address them. Finally, we combine these strategies to propose a model-independent and dataset-independent technique that improves performance on a host of molecular property prediction datasets – Open Catalyst [4], MD17 [5], QM9 [22, 20] – across different backbone GNN architectures – SchNet [23], GemNet [10], Graphormer [25].

On the OC20 IS2RE dataset, our method shows an average of 8.4% and 34.3% relative improvement on energy MAE and energy within threshold metrics, respectively, across the validation ID and OOD adsorbate splits and an average of 4.6% and 18.4% relative improvement over all validation splits. On the QM9 dataset, our method shows an average improvement of 5% in threshold accuracy. Finally, on the MD17 dataset, our method shows an average improvement of 0.17% on energy MAEs.

We utilize our technique to create a variant of GemNet [10] that achieves competitive results to the current state of the art on the OC20 dataset’s direct IS2RE prediction task.

## 2 Histogram Regression

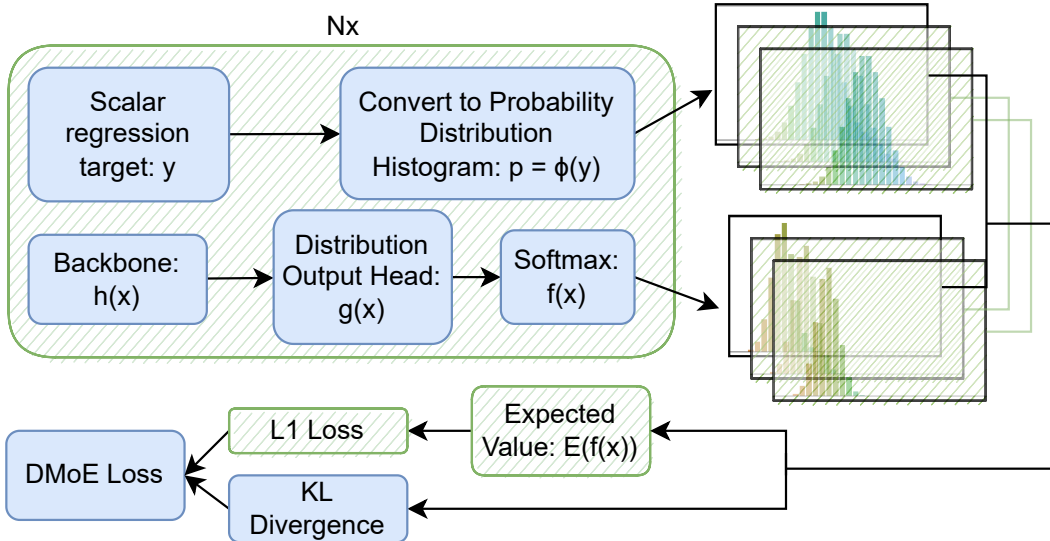


Figure 1: Overview of histogram regression. DMoE additions are highlighted in green.

For bounded regression problems, histogram regression [15], illustrated in fig. 1, is a simple and effective technique for increasing performance. Assume we have a scalar target  $y \in [y_{min}, y_{max}]$  and a backbone model  $h(x)$ . In histogram regression, instead of training a model to directly predict  $y$ , we train a model to predict a target probability distribution that we construct from  $y$ . Traditionally, this constructed target distribution is a Gaussian distribution with a mean of  $y$  and with a fixed variance,  $\sigma^2$ , set as a hyperparameter. This target distribution is then discretized to a histogram representation with a fixed number of bins,  $N$ , where each bin has a fixed width,  $w$ , and the bin boundaries are set as  $\vec{b}_i = i \times w + y_{min}$  for  $i = 1, 2, \dots, N$ . The mass at each bin,  $p_i$ , is equal to  $P(\vec{b}_i + w) - P(\vec{b}_i)$ , where  $P(x)$  is the CDF of the Gaussian distribution.

We then attach a histogram output head,  $g(x)$  to the backbone model and take the

softmax of the histogram output head, giving us the final model output,  $\hat{Y} = f(x)$ .

$$f(x) = \text{softmax}(g(x)) \quad (1)$$

$$\text{where } g(x) = \text{MLP}(h(x)) \quad (2)$$

The loss function – called the histogram loss – is then the cross entropy between the model’s predicted distribution and the induced distribution.

$$L_{HL}(\hat{Y}, Y) = - \sum_i Y_i \log(\hat{Y}_i) \quad (3)$$

Imani and White [15] provide theoretical justification for the improved performance of histogram regression over traditional regression. By comparing the norm of the loss gradient for histogram loss vs. a mean squared error loss, they show that histogram losses produce smoother, more stable gradients. We refer the reader to Sec. 3 in Imani and White [15] for a detailed exposition on this.

However, existing theoretical results are insufficient at explaining the observed strengths and drawbacks of histogram regression. Through careful empirical evaluation, we identify two primary biases that are inherent in histogram regression – 1) Distribution Quantization Error and 2) Histogram Distance Bias. Additional biases are explored in App. A.2.

## 2.1 Distribution Quantization Error

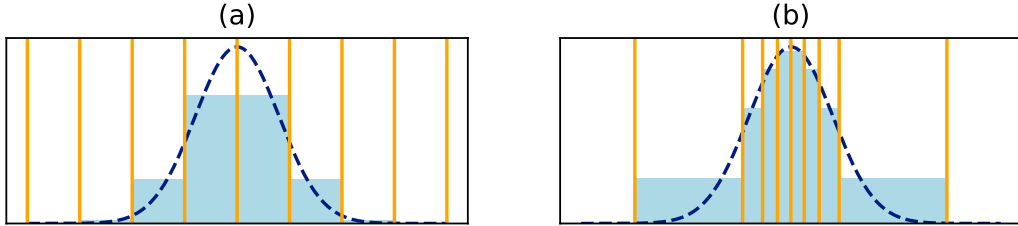


Figure 2: For a normally distributed regression target, notice how traditional uniform histograms, shown in (a), yields a much lower precision (and thus a higher error) than the histogram with normally distributed bins, shown in (b). Using eq. (11), we compute the quantization error of (a) to be 6.07 and (b) to be 2.53.

Distribution quantization error refers to the unavoidable error that comes from utilizing a discrete distributional representation for regression targets. In other words, this is quantization error of going from the induced target probability histogram to a scalar-valued target.

We empirically demonstrate this error by utilizing a threshold accuracy metric. A threshold accuracy metric is one that measures the percentage of predictions that are within a certain threshold of the true target value, rather than the absolute value of the difference between the prediction and the true target value. Intuitively, quantization error or error due to coarse resolution will contribute towards an absolute error metric but not towards binary threshold metrics (as long as predictions are within the threshold).

To address this error:

- We allow the probability distribution histogram to be non-linear. In other words, we allow the histogram bins to be non-equidistant and thus have different widths. This allows us to increase the resolution of our histograms (by using smaller bins) in intervals with higher densities of values (see fig. 2). Sec. 2.1.1 describes, in more detail, how this is achieved.

- Instead of a single output head, we use a series of output heads, where each head’s target histogram uses slightly shifted bin endpoints. Note that simply using multiple output heads – all with the same target histogram (i.e. the same bin endpoints) – is still susceptible to quantization error, so using shifted bin endpoints across output heads is essential. The multi-histogram loss value is then the (optionally weighted) mean of the loss for each individual histogram. The optimized implementation of this procedure is described in App. A.9.

### 2.1.1 Histogram Bin Distribution

Our technique allows us to adjust the bin distribution. We choose, as a hyperparameter, the histogram bin distribution to use,  $B$ . For a histogram of  $N$  bins, we use the quantile function of  $B$ ,  $Q_B$ , to construct a histogram with  $N$  equally probable bins under the distribution  $B$ .

$$\vec{b} = [0 + \epsilon, Q_B(0), Q_B(1/N), Q_B(2/N), \dots, Q_B(1 - 1/N), 1 - \epsilon] \quad (4)$$

where  $\epsilon$  is a small constant.

For our experimental results, we found that normally-distributed histogram bins yielded the best results across all evaluated datasets. Ablation studies comparing the performance of uniformly-distributed endpoints with normally-distributed endpoints can be found in Sec. 4.5.1.

## 2.2 Histogram Distance Bias

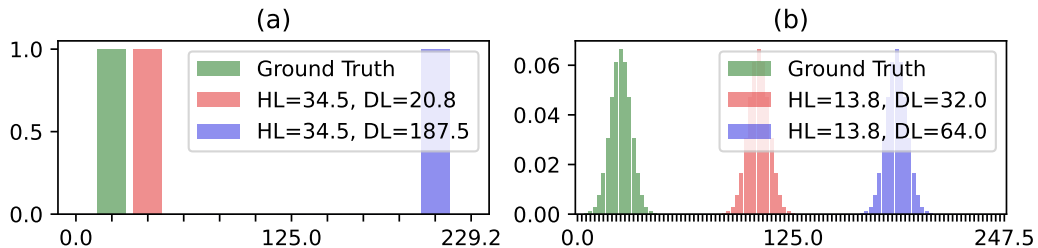


Figure 3: The model’s output is represented by the green histograms, and the red and blue histograms represent two sample model predictions. The histogram loss value (HL) and the distance-based loss metric (DL) are shown in the legend box. Note that in (a), the red histogram is much closer to the ground truth than the blue histogram, but their HL values are equal. The distance-based metric fixes this. (b) demonstrates how this phenomenon is present even if we induce a Gaussian distribution.

This refers to the error introduced by using cross entropy as our histogram loss function. Cross entropy treats every bin’s probability independently, and thus, cannot distinguish the magnitude or ‘distance’ of errors in the histogram’s prediction (see fig. 3 (a)). Existing implementations of histogram loss [15] utilize an induced Gaussian representation for the probability histogram to avoid this bias, but as demonstrated in fig. 3 (b), this technique does not fully address this bias.

To fix this error, we use an additional distance-based term in our overall loss. This loss computes the  $\ell_1$  distance between the expected value of the model’s predicted histogram and the true scalar.

$$L_{DL}(\hat{Y}, y) = \|y - \mathbb{E}(\hat{Y})\|_1 \quad (5)$$

Our final loss, then, is the combination of the histogram loss and the distance-based loss.

$$L_{DMoE}(\hat{Y}, y) = \alpha_{HL} L_{HL}(\hat{Y}, \Phi(y)) + \alpha_{DL} L_{DL}(\hat{Y}, y) \quad (6)$$

where  $\alpha_{HL}$  and  $\alpha_{DL}$  are the coefficients of the distributional and distance-based losses, respectively. These coefficients are chosen as hyperparameters, and their values can be adjusted during training according to a pre-defined schedule (see Sec. 4.5.2 for ablation studies).

### 3 Analysis

#### 3.1 Stable Gradients

We prove that DMoE produces more stable gradients by comparing the bounds of DMoE gradient norm with those of the MSE loss gradient norm. We use same notation as in Sec. 2.

**Theorem 1.** *Assume that  $g(x)$  is locally  $l$ -Lipschitz continuous w.r.t the model’s parameters,  $\theta$ :*

$$\left\| \frac{\partial g(x)}{\partial \theta} \right\| \leq l \tag{7}$$

Then, the norm of the gradient of DMoE loss w.r.t.  $\theta$  is bounded by:

$$\|\nabla_{\theta} L_{DMoE}(f(x), y)\| \leq l \|\vec{p} - f(x)\| \left[ 1 + \sqrt{2} \|f(x)\|_2 \|\vec{b}\| \right] \tag{8}$$

The proof for this theorem can be found in App. A.5.3. We make the following key observations from the gradient norm bound:

- The quantity  $\|\vec{p} - f(x)\|$  has an upper bound of 1. In practice, it should be very small as both  $\vec{p}$  and  $f(x)$  are probability vectors, and, as the model’s predictions get closer to the ground truth, this quantity approaches zero.
- The quantity  $\|f^2(x)\|_2$  is  $\ell_2$ -norm of the model’s output probability vector. It is always less than 1, and it heavily depends on our choice of induced probability distribution. The value of this quantity is maximized when the model predicts a categorical (i.e., one-hot) distribution, and is minimized when the model predicts a uniform distribution. A Gaussian-distributed histogram also produces a very small  $\ell_2$ -norm value (see fig. 4). This is consistent with our experimental observations (see App. A.8.1), which show that Gaussian induced distributions are more performant than categorical induced distributions.
- The quantity  $\|\vec{b}\|$  restricts the distance-based portion of the loss to only consider the range that is covered by the histogram. This puts a lower, more restrictive bound on the gradient norm than MSE, which has no such restriction.

Hardt et al. [14] suggests that lower gradient bounds yield lower generalization errors. We compare the bounds for the DMoE loss and the MSE loss, which has a gradient norm of  $l|f(x) - y|$ . Using the observations above, we show that the DMoE loss has a lower gradient norm bound. This is because the gradient norm of MSE is unbounded —  $f(x)$  could produce any value in  $\mathbb{R}$ . For DMoE, however, the norm of the histogram component is — at most — bounded by  $l \left[ 1 + \sqrt{2} (y_{max} - y_{min}) \right]$ . In reality, however, the values of  $\|\vec{p} - f(x)\|$  and  $\|f^2(x)\|_2$  are much lower. Using the  $\|f^2(x)\|_2$  value for the Gaussian distribution in fig. 4, our gradient norm bound would be  $l \left[ 1 + \frac{\sqrt{2}}{200} (y_{max} - y_{min}) \right]$ .

#### 3.2 Uncertainty Quantification

One natural consequence of predicting probability distributions is that we have a natural way to quantify uncertainty in our model’s predictions. In the single histogram case, this is trivially achieved by computing the entropy of the predicted histogram:  $H(\hat{Y}) = -\sum_k \hat{Y}_k \log(\hat{Y}_k)$ .

For multiple output heads, we have access to two separate natural uncertainty quantifiers: (1) the mean entropy across all output heads, and (2) the mean KL-divergence across all pairs of output heads. The former is very similar to the single histogram case and is easy to compute. The latter, however, is more difficult to compute. This is because the KL-divergence requires the two histograms to be defined on the same support, but, by definition, this is not always the case in our method. Therefore, we use a trick to compute the KL-divergence: We pick one predicted histogram,  $\hat{Y}^{(0)}$  and linearly interpolate all predicted histograms to  $\hat{Y}^{(0)}$ 's support. We can then easily compute the KL-divergence between the interpolated histograms:  $H(\hat{Y}^{(i)}, \hat{Y}^{(j)}) = -\sum_k \tau(\hat{Y}_k^{(i)}) \log \left( \frac{\tau(\hat{Y}_k^{(j)})}{\tau(\hat{Y}_k^{(i)})} \right)$ , where  $\tau(Y)$  is our interpolation function. Our uncertainty score, then, is the maximum KL divergence between any two histograms.

$$U(\hat{Y}) = \max_{i,j} [H(\hat{Y}^{(i)}, \hat{Y}^{(j)})] \quad (9)$$

Finally, we must note that both these uncertainty entropy values are in nats and thus must be scaled before being useful. In our method, we use a simple technique, where we use 10% of the validation to compute optimal shifting and scaling parameters for the uncertainty scores. The final uncertainty score is then:

$$U_{\text{adjusted}}(\hat{Y}) = \gamma U(\hat{Y}) + \delta \quad (10)$$

where  $\gamma, \delta \in \mathbb{R}$  are the scaling and shifting parameters.

## 4 Evaluation

In this section, we will evaluate models trained using DMoE loss with their baseline (i.e., models trained on L1 loss) performance. For all experiments, we will report the MAE of the targets of interest. Whenever applicable, we will also report threshold accuracies (WT), which is the percentage of targets that are correctly predicted within a given margin of error. For all experiments, this threshold is set at 0.1% of the maximum possible error (i.e.,  $0.001|y_{max} - y_{min}|$ ). Information on the training environment and the amount of compute used during training can be found in App. A.1.

### 4.1 Open Catalyst 2020: Relaxed Energy Prediction

The OC20 dataset [4] is one of the largest publicly available catalysis datasets, containing 1.2M relaxations of adsorbate-catalyst structures. For our experiments, we evaluate our technique on the Initial Structure to Relaxed Energy (IS2RE) task. This is a graph-level regression task in which the model has to estimate the relaxed energy of an adsorbate-catalyst system from an initial state. The training dataset comprises of 466k initial unrelaxed adsorbate-catalyst structures paired with relaxed energies.

We evaluate our method with four different backbone GNNs – SchNet [23], DimeNet++ [8, 9], GemNet-dT [10], and 3D Graphormer [30, 25]. Table 1 shows validation results for all backbone models when trained on the full OC20 IS2RE dataset. For the GemNet and 3D Graphormer models, we evaluate these methods with and without the relaxed position prediction auxiliary task from Shi et al. [25]. Our results demonstrate some very clear trends. First, across nearly all backbone models, using DMoE shows substantial improvements over the baseline, HL and DL variants. For 3D Graphormer, the baseline performs about the same as DMoE in energy MAE, but DMoE performs significantly better on the Energy within Threshold (EwT) metric. Second, the addition of the relaxed position prediction auxiliary task improves performance across GemNet-dT and 3D Graphormer, but it does not change the observed trends on EwT with DMoE. Third, DMoE is not effective on the out-of-distribution adsorbate (OOD Ads) and OOD Both splits. It neither hurts nor improves performance. We discuss this further in Sec. 4.6.1.

Table 1: Accuracy scores across the different validation splits in the OC20 IS2RE dataset. For each model, we evaluate using the baseline L1 loss, the histogram loss (HL-only), the distance-based loss (DL-only), and the Distributional Mixture of Experts Loss (DMoE). Energy MAEs are reported in eV.

		ID		OOD Ads		OOD Cat		OOD Both	
		MAE	EwT	MAE	EwT	MAE	EwT	MAE	EwT
SchNet	Baseline	0.954	1.9%	1.045	1.5%	0.925	1.8%	0.964	1.5%
	HL-only	0.713	3.0%	0.910	1.7%	0.706	3.0%	0.822	1.8%
	DL-only	1.780	0.8%	1.701	0.9%	1.788	0.8%	1.586	0.9%
	DMoE	0.702	3.0%	0.914	1.7%	0.695	3.3%	0.820	1.8%
DimeNet++	Baseline	0.675	3.1%	0.774	2.1%	0.665	3.1%	0.720	2.2%
	HL-only	0.671	3.3%	0.901	1.9%	0.647	3.8%	0.806	2.1%
	DL-only	1.750	0.8%	1.863	0.7%	1.746	0.9%	1.696	0.8%
	DMoE	0.652	3.6%	0.790	2.1%	0.635	4.0%	0.725	2.2%
GemNet-dT	Baseline	0.610	3.6%	0.795	2.2%	0.626	3.5%	0.770	2.2%
	HL-only	0.571	5.0%	0.821	2.0%	0.579	5.2%	0.738	2.3%
	DL-only	2.253	0.8%	1.940	0.7%	2.208	0.7%	1.674	0.9%
	DMoE	0.557	5.0%	0.752	2.4%	0.560	4.9%	0.676	2.5%
	Baseline + Pos	0.476	5.7%	0.563	3.5%	0.482	6.0%	0.506	3.6%
	DMoE + Pos	0.450	7.8%	0.574	3.5%	0.459	7.4%	0.513	3.6%
3D Graphormer	Baseline	0.528	4.9%	0.705	2.4%	0.531	4.7%	0.645	2.7%
	HL-only	0.560	5.8%	0.824	2.1%	0.567	5.7%	0.735	2.3%
	DL-only	0.529	5.3%	0.709	2.6%	0.531	5.2%	0.632	2.5%
	DMoE	0.537	6.0%	0.785	2.3%	0.545	5.8%	0.709	2.5%
	Baseline + Pos	0.451	6.5%	0.613	2.8%	0.466	6.5%	0.560	3.0%
	DMoE + Pos	0.457	7.3%	0.712	2.8%	0.469	7.0%	0.623	3.2%
GemNet*	DMoE + Pos	<b>0.389</b>	<b>10.1%</b>	<b>0.544</b>	<b>4.9%</b>	<b>0.395</b>	<b>9.3%</b>	<b>0.486</b>	<b>5.4%</b>

To fully demonstrate the effectiveness of DMoE, we design a variant of the GemNet model, which we will refer to as GemNet\*, with the following changes: 1) We increase the number of blocks to 12 and repeat these blocks 2 times. 2) We use layer norm before each interaction block. 3) Instead of using one output block for each interaction block, we use a single output block at the end of the model to output the energy probability distribution. 4) Finally, we apply Gaussian augmentation to the atoms’ positions. We evaluate this model on the OC20 IS2RE test set.

Table 2 shows results for some of the current state-of-the-art models, as well as other baselines, for the OC20 IS2RE test set. Similar to the previous results, we see that the DMoE model performs significantly well on the ID and OOD Cat splits, but its performance drops in the OOD Ads and OOD Both splits.

Table 2: OC20 IS2RE test results. Energy MAEs are reported in eV.

	ID		OOD Ads		OOD Cat		OOD Both	
	MAE	EwT	MAE	EwT	MAE	EwT	MAE	EwT
GemNet-OC (Relaxation) [11]	<b>0.331</b>	<b>18.4%</b>	<b>0.336</b>	<b>15.2%</b>	<b>0.379</b>	<b>14.2%</b>	0.344	<b>12.1%</b>
GemNet-XL (Relaxation) [27]	0.376	13.3%	0.368	10.0%	0.402	11.6%	<b>0.338</b>	9.7%
GemNet-T (Relaxation) [10]	0.390	12.4%	0.391	9.1%	0.434	10.1%	0.384	7.9%
SpinConv (Relaxation) [26]	0.421	9.4%	0.438	7.5%	0.458	8.2%	0.420	6.6%
DimeNet++ (Relaxation) [9, 8]	0.503	6.6%	0.543	4.3%	0.579	5.1%	0.611	3.9%
CGCNN (Direct) [29]	0.615	3.4%	0.916	1.9%	0.622	3.1%	0.851	2.0%
SchNet (Direct) [23]	0.639	3.0%	0.734	2.3%	0.662	2.9%	0.704	2.2%
NequiP (Direct) [1]	0.602	3.2%	0.784	2.2%	0.619	3.1%	0.736	2.1%
PaiNN (Direct) [24]	0.575	3.5%	0.783	2.0%	0.604	3.5%	0.743	2.3%
DimeNet++ (Direct) [9, 8]	0.562	4.3%	0.725	2.1%	0.576	4.1%	0.661	2.4%
SphereNet (Direct) [18]	0.563	4.5%	0.703	2.3%	0.571	4.1%	0.638	2.4%
SEGNN (Direct) [2]	0.533	5.4%	0.692	2.5%	0.537	4.9%	0.679	2.6%
Noisy Nodes (Direct) [13]	0.422	9.1%	<b>0.568</b>	<b>4.3%</b>	0.437	8.0%	<b>0.465</b>	<b>4.6%</b>
3D Graphormer (Direct) [30, 25]	0.398	9.0%	0.572	3.5%	0.417	8.2%	0.503	3.8%
GemNet*+DMoE (Direct, Ours)	<b>0.390</b>	<b>10.1%</b>	0.640	3.6%	<b>0.401</b>	<b>8.9%</b>	0.576	3.9%

## 4.2 MD17: Molecular Dynamics

MD17 [5] contains energies and forces for molecular dynamics trajectories of eight organic molecules. The task is two-fold: (1) predicting the energy of a molecular system, and (2) predicting the force of each atom in the system. For our experiments, we demonstrate results on the 1k and 50k splits of the MD17 dataset. However, while the 50k split provides much more training data, it does not guarantee independent samples in the test set and is therefore much less reliable.

We evaluate DMoE using two separate backbone GNNs, one for each method of estimating forces – SchNet with forces calculated as negative gradient of the energy w.r.t atom positions, and GemNet-dT with the direct-force output head. For each, we report the energy and force MAE values for the baseline (trained on L1 loss) with the DMoE method applied to the energy outputs.

Table 3: Validation scores across all different molecules in the 1k and 50k splits of the MD17 dataset. Energy MAEs are reported in meV, and force MAEs are reported in meV/Å.

	GemNet-dT				SchNet			
	Baseline		DMoE		Baseline		DMoE	
	Energy	Forces	Energy	Forces	Energy	Forces	Energy	Forces
Aspirin (1k)	<b>105.3</b>	45.6	109.9	<b>45.5</b>	152.8	<b>72.2</b>	<b>149.7</b>	79.8
Benzene (1k)	27.9	<b>14.0</b>	<b>21.9</b>	15.3	70.5	<b>18.3</b>	<b>70.4</b>	18.7
Ethanol (1k)	<b>19.8</b>	<b>23.9</b>	24.1	25.1	116.6	<b>38.3</b>	<b>116.5</b>	42.0
Malonaldehyde (1k)	<b>52.2</b>	<b>42.8</b>	56.1	44.1	113.2	<b>62.0</b>	<b>112.7</b>	64.0
Naphthalene (1k)	59.6	<b>23.3</b>	<b>54.7</b>	30.9	146.4	<b>39.5</b>	<b>146.2</b>	42.9
Salicylic (1k)	<b>75.3</b>	<b>39.8</b>	83.4	41.4	144.7	61.9	<b>143.6</b>	<b>60.8</b>
Toluene (1k)	58.8	<b>25.2</b>	<b>56.8</b>	32.6	132.0	<b>38.9</b>	<b>131.4</b>	42.6
Uracil (1k)	<b>54.9</b>	<b>36.6</b>	60.7	39.5	127.7	<b>56.2</b>	<b>127.3</b>	57.4
Aspirin (50k)	6.9	3.3	<b>5.0</b>	<b>2.9</b>	151.8	<b>24.2</b>	<b>150.7</b>	26.0
Benzene (50k)	<b>1.3</b>	<b>6.0</b>	1.4	6.3	74.3	<b>11.1</b>	<b>74.0</b>	14.2
Ethanol (50k)	<b>0.6</b>	<b>0.9</b>	1.0	1.3	119.9	<b>7.0</b>	<b>119.4</b>	9.9
Malonaldehyde (50k)	<b>1.0</b>	<b>1.2</b>	1.5	2.2	119.7	<b>13.0</b>	<b>119.3</b>	16.2
Naphthalene (50k)	1.8	<b>1.2</b>	<b>1.7</b>	1.3	142.9	<b>12.8</b>	<b>142.1</b>	15.7
Salicylic (50k)	3.8	<b>2.4</b>	<b>3.2</b>	2.6	140.5	<b>18.7</b>	<b>140.0</b>	22.5
Toluene (50k)	1.6	<b>1.1</b>	<b>1.4</b>	<b>1.1</b>	128.2	<b>14.2</b>	<b>127.1</b>	18.9
Uracil (50k)	1.3	<b>1.3</b>	<b>1.2</b>	1.4	128.8	<b>14.1</b>	<b>127.4</b>	17.7

Table 3 shows the MD17 results for the SchNet and GemNet-dT backbone models. For the SchNet model, DMoE performs better on energy predictions but worse on force predictions. We believe that the decrease in force prediction performance is due to the fact that SchNet calculates forces by differentiating the energy with respect to atom positions, and, as a result, any quantization errors in the energy predictions will also propagate to the force predictions. Similarly for the GemNet model, we see improved energy prediction performance across about half of the molecules but decreased force prediction performance overall.

## 4.3 QM9: Molecular Property Prediction

QM9 [22, 20] is a dataset which contains quantum chemical properties of 134,000 organic molecules made up of CHNOF atoms. For this dataset, we train the MXMNet [31] as our backbone. To keep the methodology consistent with MXMNet, we only use atomization energies for  $U_0$ ,  $U$ ,  $H$ , and  $G$ . For each target property, we train a separate model for 100 epochs and report the best validation results.

Table 4 shows QM9 validation scores for the MXMNet backbone model. We see very promising results — with at least a 4% improvement in the threshold metric — across multiple different targets, including  $\mu$ ,  $e_{HOMO}$ ,  $e_{LUMO}$  and  $\Delta e$ . For the rest of the targets, both models seem to produce similarly accurate results, from a threshold metric perspective.



Table 4: Validation scores for the MXMNet backbone model on the QM9 dataset

	Baseline		DMoE	
	MAE	WT	MAE	WT
$\mu$ (D)	0.0444	56.9%	<b>0.0397</b>	<b>60.9%</b>
$a$ ( $a_0^3$ )	<b>0.0624</b>	<b>95.9%</b>	0.0716	95.1%
$e_{HOMO}$ (eV)	0.0290	26.5%	<b>0.0275</b>	<b>33.1%</b>
$e_{LUMO}$ (eV)	0.0227	<b>40.2%</b>	<b>0.0225</b>	39.9%
$\Delta e$ (eV)	0.0456	29.8%	<b>0.0414</b>	<b>36.4%</b>
$R^2$ ( $a_0^3$ )	1.3034	93.9%	<b>0.9813</b>	<b>95.9%</b>
$ZPVE$ (eV)	0.0015	99.1%	<b>0.0014</b>	<b>99.5%</b>
$U_0$ (eV)	<b>0.0226</b>	<b>98.9%</b>	0.0236	<b>98.9%</b>
$U$ (eV)	<b>0.0143</b>	<b>99.7%</b>	0.0235	98.9%
$H$ (eV)	<b>0.0144</b>	<b>99.6%</b>	0.0228	99.0%
$G$ (eV)	<b>0.0138</b>	<b>99.6%</b>	0.0223	98.7%
$c_p$ (cal/mol.K)	<b>0.0253</b>	<b>82.7%</b>	0.0272	80.5%

Table 5: Uncertainty metrics for GemNet-dT evaluated on the OC20 ID validation split

	MACE	RMSCE	MA
Ensemble	0.2752	0.3119	0.2780
Ensemble + IR Recal	0.0237	0.0334	0.0240
DMoE-Entropy	0.0427	0.0668	0.0431
DMoE-Entropy + IR Recal	0.0116	0.0303	0.0117
DMoE-KL	0.0542	0.0664	0.0547
DMoE-KL + IR Recal	<b>0.0057</b>	<b>0.0165</b>	<b>0.0057</b>

## 4.4 Uncertainty Quantification

To evaluate the reliability of the uncertainties computed, we compare the uncertainties predicted by GemNet\* to the uncertainties predicted by an ensemble of 5 baseline GemNet-dT models, both trained with the position-prediction auxiliary task. All of these models are trained on the full OC20 IS2RE dataset and are evaluated on the ID validation split. For each model, we report the mean absolute calibration error (MACE), the root mean squared calibration error (RMSE), and the miscalibration area (MA). All methods are shown with and without isotonic regression recalibration technique proposed by Kuleshov et al. [16]. For this purpose, we set aside 10% of the evaluation data split for recalibration. For the DMoE uncertainty methods, the data used for isotonic regression recalibration and for our readjustment procedure are the same (i.e., the same 10% of the evaluation data split).

Table 5 shows these uncertainty results. There are two key observations from these results: 1) The DMoE KL method provides excellent uncertainty metrics, outperforming all other methods. 2) While the DMoE entropy and KL methods can provide acceptable uncertainty metrics without the need for isotonic regression recalibration, performing this recalibration further the uncertainty estimates.

## 4.5 Ablations

### 4.5.1 Bin Distribution

We investigate the impact of changing the bin distribution hyperparameters. Specifically, we experiment with changing the number of histograms, the number of bins in each histogram, and the bin distribution (i.e., uniform or Gaussian). All experiments are done on the DMoE+Pos version of the model from table 1 and are evaluated on the ID validation split of the OC20 dataset. Table 7 shows these results. We see, clearly, that using a Gaussian bin distribution produces substantially better results. Increasing the number of histograms seems to help with the uniform bin distributions, but not with the Gaussian bin distribution. Conversely, increasing the number of bins in each histogram seems to help with the Gaussian bin distribution, but not with the uniform bin distribution.

### 4.5.2 Loss Coefficients

We investigate the effect of the histogram and distance-based loss coefficients. To do this, we compute a normalizing constant such that the magnitude of the HL and DL losses are equal. Then, we experiment with different values for these coefficients. The results can be found in table 6. Our primary observation was that a higher histogram loss coefficient  $\alpha_{HL}$  yields better results and faster training at the beginning of training, but as training progresses, the biases outlined in Sec. 2 begin to show their effects. To demonstrate this, we launch a variant where we schedule the loss coefficients from  $\alpha_{HL} = 0.9, \alpha_{DL} = 0.1$  to

Table 6: The impact of different HL and DL coefficients on the performance of the GemNet+Pos model on the ID split of OC20

$\alpha_{HL}$	$\alpha_{DL}$	E-MAE	EWT
1.00	0.00	0.455	<b>8.3%</b>
0.90	0.10	0.457	8.0%
0.75	0.25	0.459	8.1%
0.50	0.50	0.457	8.1%
0.25	0.75	0.462	7.9%
0.10	0.90	0.473	7.3%
0.00	1.00	2.253	0.8%
Scheduled		<b>0.450</b>	7.8%

$\alpha_{HL} = 0.05, \alpha_{DL} = 0.95$  over the course of 20 epochs. The results for this run are displayed on the ‘‘Scheduled’’ row of table 6.

## 4.6 Analysis

### 4.6.1 Effectiveness on OOD data

One apparent drawback of our technique seems to be its lack of performance on OOD adsorbate and OOD both data on the OC20 dataset (Table 2). We attribute this to two reasons:

1. Direct models, in general, seem to perform poorly on OOD adsorbate and OOD both. This might be because relaxation-based models have more physical intuition embedded in them, whereas the direct models tend to overfit to the distribution they’re trained on.
2. Our method defines the histogram bin distribution over the range of possible target values in the train set. This selection of bin distribution introduces a bias in the model. As a result, if the OOD data is not distributed similarly to the training data, the model’s histogram distribution will be suboptimal. This argument can be supported by examining the target distribution histograms of the train and OOD splits (see App. A.7).

### 4.6.2 Quantization Error and Impact of Distance-Based Loss

Comparing MAE and EwT in Table 1, we notice that the histogram loss leads to significantly better EwT but worse MAE. We suspect that this is due to the quantization error described in Sec. 2.1. Adding the distance-based loss (the DMoE rows in table 1) shows improvements in both MAE and EwT. Scheduling the loss coefficients, as shown in Sec. 4.5.2, attains the best results, suggesting that the distance-based loss contributes to the model’s ability to learn the distribution of the target values.

## 5 Conclusion

In this paper, we proposed Distributional Mixture of Experts, a method for enhancing regression performance by learning distributional representations of target values. We show that this method is effective for molecular regression tasks, demonstrating consistent improvements over the baselines across various datasets (OC20, MD17, QM9) and backbone GNN architectures.

Developing better methods for molecular regression tasks can have many positive consequences, enabling progress in the many subfields of chemistry, such as drug discovery and synthesis and development and discovery of new battery technologies. However, unintended

Table 7: Validation results for running GemNet+Pos on the ID split of the OC20 IS2RE dataset, varying the bin distribution, number of histograms, and number of bins

	$N_H \times N_B$	Energy MAE	EWT
Uniform	32x2048	0.467	6.5%
	64x1024	<b>0.464</b>	<b>7.2%</b>
	256x256	0.466	7.1%
Gaussian	32x2048	<b>0.454</b>	<b>8.3%</b>
	64x1024	0.455	7.9%
	256x256	0.459	7.3%

consequences of ML for molecular property prediction must also be considered – hypothetically, similar technologies can be used to study explosive materials and their properties, which can be used to develop weapons.

## References

- [1] Simon Batzner, Tess E Smidt, Lixin Sun, Jonathan P Mailoa, Mordechai Kornbluth, Nicola Molinari, and Boris Kozinsky. Se (3)-equivariant graph neural networks for data-efficient and accurate interatomic potentials. *arXiv preprint arXiv:2101.03164*, 2021.
- [2] Johannes Brandstetter, Rob Hesselink, Elise van der Pol, Erik Bekkers, and Max Welling. Geometric and physical quantities improve e (3) equivariant message passing. *arXiv preprint arXiv:2110.02905*, 2021.
- [3] Tianle Cai, Shengjie Luo, Keyulu Xu, Di He, Tie-Yan Liu, and Liwei Wang. Graphnorm: A principled approach to accelerating graph neural network training, 2020. URL <https://arxiv.org/abs/2009.03294>.
- [4] Lowik Chanussot\*, Abhishek Das\*, Siddharth Goyal\*, Thibaut Lavril\*, Muhammed Shuaibi\*, Morgane Riviere, Kevin Tran, Javier Heras-Domingo, Caleb Ho, Weihua Hu, Aini Palizhati, Anuroop Sriram, Brandon Wood, Junwoong Yoon, Devi Parikh, C. Lawrence Zitnick, and Zachary Ulissi. Open catalyst 2020 (oc20) dataset and community challenges. *ACS Catalysis*, 2021. doi: 10.1021/acscatal.0c04525.
- [5] Stefan Chmiela, Alexandre Tkatchenko, Huziel E Sauceda, Igor Poltavsky, Kristof T Schütt, and Klaus-Robert Müller. Machine learning of accurate energy-conserving molecular force fields. *Science advances*, 3(5):e1603015, 2017.
- [6] Tien Huu Do, Duc Minh Nguyen, Giannis Bekoulis, Adrian Munteanu, and Nikos Deligiannis. Graph convolutional neural networks with node transition probability-based message passing and DropNode regularization. *Expert Systems with Applications*, 174: 114711, jul 2021. doi: 10.1016/j.eswa.2021.114711. URL <https://doi.org/10.1016%2Fj.eswa.2021.114711>.
- [7] David K. Duvenaud, Dougal Maclaurin, Jorge Aguilera-Iparraguirre, Rafael Gómez-Bombarelli, Timothy Hirzel, Alán Aspuru-Guzik, and Ryan P. Adams. Convolutional Networks on Graphs for Learning Molecular Fingerprints. In *NeurIPS*, 2015.
- [8] Johannes Gasteiger, Shankari Giri, Johannes T Margraf, and Stephan Günnemann. Fast and uncertainty-aware directional message passing for non-equilibrium molecules. *arXiv preprint arXiv:2011.14115*, 2020.
- [9] Johannes Gasteiger, Janek Groß, and Stephan Günnemann. Directional message passing for molecular graphs. *arXiv preprint arXiv:2003.03123*, 2020.
- [10] Johannes Gasteiger, Florian Becker, and Stephan Günnemann. GemNet: Universal directional graph neural networks for molecules. *arXiv preprint arXiv:2106.08903*, 2021.
- [11] Johannes Gasteiger, Muhammed Shuaibi, Anuroop Sriram, Stephan Günnemann, Zachary Ulissi, C Lawrence Zitnick, and Abhishek Das. How do graph networks generalize to large and diverse molecular systems? *arXiv preprint arXiv:2204.02782*, 2022.
- [12] Justin Gilmer, Samuel S. Schoenholz, Patrick F. Riley, Oriol Vinyals, and George E. Dahl. Neural Message Passing for Quantum Chemistry. In *ICML*, 2017.

- [13] Jonathan Godwin, Michael Schaarschmidt, Alexander Gaunt, Alvaro Sanchez-Gonzalez, Yulia Rubanova, Petar Veličković, James Kirkpatrick, and Peter Battaglia. Simple gnn regularisation for 3d molecular property prediction and beyond. In *ICLR*, 2022.
- [14] Moritz Hardt, Ben Recht, and Yoram Singer. Train faster, generalize better: Stability of stochastic gradient descent. In *International conference on machine learning*, pages 1225–1234. PMLR, 2016.
- [15] Ehsan Imani and Martha White. Improving regression performance with distributional losses. In *International Conference on Machine Learning*, pages 2157–2166. PMLR, 2018.
- [16] Volodymyr Kuleshov, Nathan Fenner, and Stefano Ermon. Accurate uncertainties for deep learning using calibrated regression. In *International conference on machine learning*, pages 2796–2804. PMLR, 2018.
- [17] Guohao Li, Chenxin Xiong, Ali Thabet, and Bernard Ghanem. Deepergcn: All you need to train deeper gcns, 2020. URL <https://arxiv.org/abs/2006.07739>.
- [18] Yi Liu, Limei Wang, Meng Liu, Xuan Zhang, Bora Oztekin, and Shuiwang Ji. Spherical message passing for 3d graph networks. *arXiv preprint arXiv:2102.05013*, 2021.
- [19] Gabriel Pereyra, G. Tucker, Jan Chorowski, Lukasz Kaiser, and Geoffrey E. Hinton. Regularizing neural networks by penalizing confident output distributions. *ArXiv*, abs/1701.06548, 2017.
- [20] Raghunathan Ramakrishnan, Pavlo O Dral, Matthias Rupp, and O Anatole von Lilienfeld. Quantum chemistry structures and properties of 134 kilo molecules. *Scientific Data*, 1, 2014.
- [21] Yu Rong, Wenbing Huang, Tingyang Xu, and Junzhou Huang. Droppedge: Towards deep graph convolutional networks on node classification, 2019. URL <https://arxiv.org/abs/1907.10903>.
- [22] Lars Ruddigkeit, Ruud van Deursen, Lorenz C. Blum, and Jean-Louis Reymond. Enumeration of 166 billion organic small molecules in the chemical universe database gdb-17. *Journal of Chemical Information and Modeling*, 52(11):2864–2875, 2012. doi: 10.1021/ci300415d. URL <https://doi.org/10.1021/ci300415d>. PMID: 23088335.
- [23] Kristof Schütt, Pieter-Jan Kindermans, Huziel Enoc Saucedo Felix, Stefan Chmiela, Alexandre Tkatchenko, and Klaus-Robert Müller. Schnet: A continuous-filter convolutional neural network for modeling quantum interactions. *Advances in neural information processing systems*, 30, 2017.
- [24] Kristof Schütt, Oliver Unke, and Michael Gastegger. Equivariant message passing for the prediction of tensorial properties and molecular spectra. In *International Conference on Machine Learning*, pages 9377–9388. PMLR, 2021.
- [25] Yu Shi, Shuxin Zheng, Guolin Ke, Yifei Shen, Jiacheng You, Jiyan He, Shengjie Luo, Chang Liu, Di He, and Tie-Yan Liu. Benchmarking graphormer on large-scale molecular modeling datasets. *arXiv preprint arXiv:2203.04810*, 2022.
- [26] Muhammed Shuaibi, Adeesh Kolluru, Abhishek Das, Aditya Grover, Anuroop Sriram, Zachary Ulissi, and C Lawrence Zitnick. Rotation invariant graph neural networks using spin convolutions. *arXiv preprint arXiv:2106.09575*, 2021.
- [27] Anuroop Sriram, Abhishek Das, Brandon M Wood, Siddharth Goyal, and C Lawrence Zitnick. Towards training billion parameter graph neural networks for atomic simulations. *arXiv preprint arXiv:2203.09697*, 2022.

- [28] Christian Szegedy, Vincent Vanhoucke, Sergey Ioffe, Jon Shlens, and Zbigniew Wojna. Rethinking the inception architecture for computer vision. In *Proceedings of the IEEE Conference on Computer Vision and Pattern Recognition (CVPR)*, June 2016.
- [29] Tian Xie and Jeffrey C Grossman. Crystal graph convolutional neural networks for an accurate and interpretable prediction of material properties. *Physical review letters*, 120(14):145301, 2018.
- [30] Chengxuan Ying, Tianle Cai, Shengjie Luo, Shuxin Zheng, Guolin Ke, Di He, Yanming Shen, and Tie-Yan Liu. Do transformers really perform badly for graph representation? *Advances in Neural Information Processing Systems*, 34, 2021.
- [31] Shuo Zhang, Yang Liu, and Lei Xie. Molecular mechanics-driven graph neural network with multiplex graph for molecular structures. *arXiv preprint arXiv:2011.07457*, 2020.
- [32] Lingxiao Zhao and Leman Akoglu. Pairnorm: Tackling oversmoothing in gnns, 2019. URL <https://arxiv.org/abs/1909.12223>.
- [33] Kaixiong Zhou, Xiao Huang, Yuening Li, Daochen Zha, Rui Chen, and Xia Hu. Towards deeper graph neural networks with differentiable group normalization, 2020. URL <https://arxiv.org/abs/2006.06972>.

## A Appendix

### A.1 Implementation, Experimental Setup, and Train Times

In this section, we will describe the training hardware and the total training time for all trained models. All models are programmed in Python using the PyTorch library [40]. All model and training code will be open sourced with MIT license upon acceptance.

#### A.1.1 GemNet Auxiliary Position

For our GemNet-dT [10] experiments, we experiment with a variant that uses the auxiliary position prediction task from Ying et al. [30]. To do this, we re-purpose the force output head of GemNet-dT to predict positions instead. This deviates from the original author’s implementation, but it yields improved predictions (see table 1).

#### A.1.2 PaiNN and NequIP Models

Our PaiNN [24] and NequIP [1] implementations contain one minor difference from the original implementation: The data normalization scheme is different to account for the adsorption energy reference used in OC20 [4].

#### A.1.3 OC20 Models

Table 8 shows the training times (in hours) for the models in table 1. All models are trained on 16 NVIDIA Tesla V100 Volta 32 GB GPUs. Training is stopped either after 100 epochs or once the model converges (i.e., using early stopping). The training time for GemNet\* model in table 2 is the same as the one shown for GemNet\* in table 8.

For table 5, the total train time of the GemNet\*-DMoE model is 115.28 hours, and the total train time of the baseline GemNet ensemble is 662.37 hours.

Table 9 shows the train times for the models of table 6.

Table 10 shows the train times for the models of table 7.

Table 11 shows the train times for the models of table 15.

Table 12 shows the train times for the models of table 16.

Table 8: Training times (in hours) for the models in table 1

		Train Time (Hours)
SchNet	Baseline	4.40
	HL	3.28
	DL	0.29
	DMoE	4.61
DimeNet++	Baseline	14.58
	HL	12.56
	DL	0.37
	DMoE	12.60
GemNet-dT	Baseline	5.07
	HL	3.18
	DL	5.34
	DMoE	2.54
	Baseline + Pos	7.12
	DMoE + Pos	16.40
3D Graphormer	Baseline	63.35
	HL	13.26
	DL	63.53
	DMoE	38.49
GemNet*	Baseline + Pos	81.55
	DMoE + Pos	88.64
	DMoE + Pos	115.28

Table 9: Training times (in hours) for the models in table 6

$\alpha$	$\beta$	Train Time
1.00	0.00	16.24
0.90	0.10	9.32
0.75	0.25	9.67
0.50	0.50	11.06
0.25	0.75	11.45
0.10	0.90	4.18
0.00	1.00	-
	Scheduled	16.40

Table 10: Training times (in hours) for the models in table 7

		Train Time
Uniform	32x2048	7.35
	64x1024	8.86
	256x256	6.28
Normal	32x2048	6.98
	64x1024	5.97
	256x256	5.41

Table 11: Training times (in hours) for the models in table 15

		Normal Bin Distribution	Uniform Bin Distribution
Normal	$\sigma = 0.5\mathbb{E}[w]$	8.26	9.27
	$\sigma = 1\mathbb{E}[w]$	10.24	8.12
	$\sigma = 1.5\mathbb{E}[w]$	9.30	6.60
	$\sigma = 2\mathbb{E}[w]$	14.99	6.05
	$\sigma = 5\mathbb{E}[w]$	6.78	6.65
Laplace	$\sigma = 10\mathbb{E}[w]$	6.81	7.45
K-Categorical	$b = 1\mathbb{E}[w]$	10.79	3.29
Categorical	$k = 3$	5.72	5.37
		16.01	7.56

Table 12: Training times (in hours) for the models in table 16

		Train Time
L1 Loss		6.58
L2 Loss		6.62
Smooth L1 Loss		7.12
DMoE		21.52

### A.1.4 MD17 Models

Table 13 shows the training times (in hours) for the models in table 3. All models are trained on a single NVIDIA Tesla V100 Volta 32 GB GPU. Training is stopped either after 100 epochs or once the model converges (i.e., using early stopping).

Table 13: Training times (in hours) for models in table 3

	GemNet		SchNet	
	Baseline	Distributional	Baseline	Distributional
Aspirin (1k)	0.47	0.50	0.49	0.50
Benzene (1k)	0.83	0.60	0.48	0.62
Ethanol (1k)	1.62	1.80	0.44	0.53
Malonaldehyde (1k)	0.66	0.62	0.46	0.59
Naphthalene (1k)	0.82	0.52	0.46	0.54
Salicylic (1k)	0.51	0.49	0.48	0.54
Toluene (1k)	0.66	0.54	0.48	0.69
Uracil (1k)	0.64	0.50	0.49	0.53
Aspirin (50k)	15.62	24.28	14.96	16.84
Benzene (50k)	25.77	12.70	15.46	14.85
Ethanol (50k)	28.10	17.24	13.73	16.01
Malonaldehyde (50k)	18.06	17.01	14.47	14.32
Naphthalene (50k)	16.78	33.13	15.30	15.97
Salicylic (50k)	26.41	29.96	14.84	15.19
Toluene (50k)	28.61	33.58	14.92	13.15
Uracil (50k)	26.94	27.74	14.51	13.93

### A.1.5 QM9 Models

Table 14 shows the training times (in hours) for the models in table 4. All models are trained on a single NVIDIA Tesla V100 Volta 32 GB GPU. Training is stopped either after 100 epochs or once the model converges (i.e., using early stopping).

Table 14: Training times (in hours) for the models in table 4

	Baseline	Distributional
$\mu$ (D)	4.58	6.29
$a$ ( $a_0^3$ )	5.07	6.04
$e_{HOMO}$ (eV)	5.36	5.46
$e_{LUMO}$ (eV)	4.59	5.77
$\Delta e$ (eV)	5.27	5.79
$R^2$ ( $a_0^2$ )	4.73	5.65
$ZPVE$ (eV)	4.99	5.81
$U_0$ (eV)	5.95	5.77
$U$ (eV)	4.70	5.63
$H$ (eV)	4.54	5.63
$G$ (eV)	5.01	5.59
$c_v$ (cal/mol.K)	4.46	5.61

## A.2 Additional Biases

In addition to the biases outlined in Sec. 2, we identify the following additional biases in the histogram regression technique in this section.

### A.2.1 Induced Distribution Bias

This refers to the bias of using a Gaussian distribution (or any other induced distribution) to represent the underlying scalar target value. In other words, this is the bias of assuming some distributional representation of a scalar target. In cases where this bias is present, we may observe a decreasing cross-entropy loss but an increasing L1 loss.

Our distance-based loss term helps alleviate this bias. Moreover, the  $\alpha_{HL}$  and  $\alpha_{DL}$  coefficients can be adjusted to minimize this bias. Empirically, we found that starting

scheduling the coefficients such that  $\alpha_{HL}$  is higher at the beginning of training (e.g.,  $\alpha_{HL} = 2.0$  and  $\alpha_{DL} = 1.0$ ) and falls to a very low value as training progresses (e.g.,  $\alpha_{HL} = 0.1$  and  $\alpha_{DL} = 1.0$ ) produces the best results (see table 6).

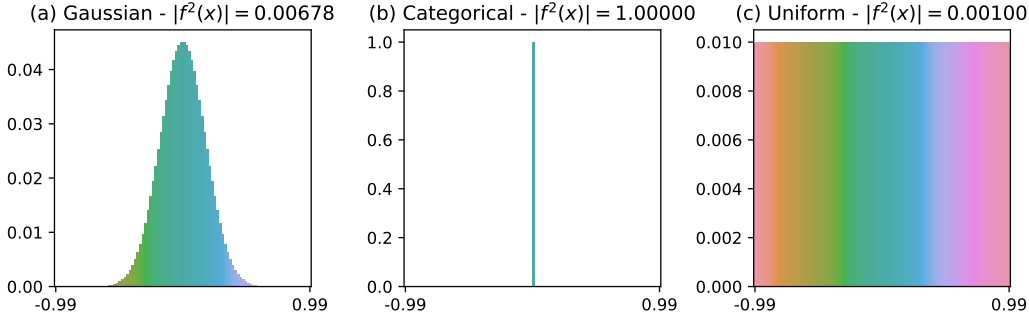


Figure 4:  $\|f^2(x)\|_2$  values for example Gaussian, Categorical, and Uniform distributions.

### A.3 Quantization Error Formula

To calculate the distribution quantization error of a histogram, shown in fig. 2, we use the following formula:

$$E_Q(Y, B) = \int_{B_i}^{B^{i+1}} |f(x) - Y_i| \cdot f(x) dx \quad (11)$$

where  $f(x)$  is the induced distribution’s continuous PDF,  $B$  is the histogram’s bin endpoints, and  $Y$  is the bin values for the histogram we are evaluating.

### A.4 Choosing Bin Distributions for Multiple Histograms

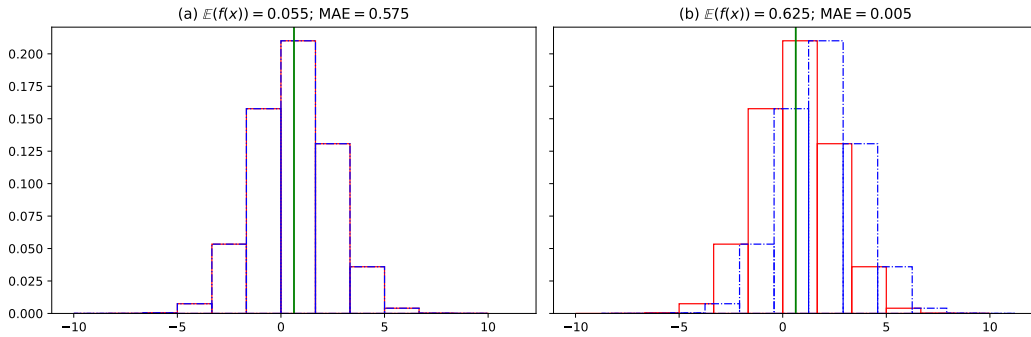


Figure 5: For each figure, the two output histograms are displayed in red and blue. The ground-truth value is displayed by the green line. (a) shows a multi-histogram scenario with uniform bin distributions where the two output histograms share the bin endpoint. (b) shows a multi-histogram scenario where the two output histograms’ bin endpoint distributions are adjusted using eq. (13).

When we use multiple output histograms, simply defining new histograms on the same bin distribution (as shown in fig. 5 (a) and fig. 6 (b)) does not help reduce our quantization error. Instead, we must vary each histogram’s bin distribution so that each new output head helps reduce our quantization error. Figure 5 (b) shows an example of this for uniformly distributed



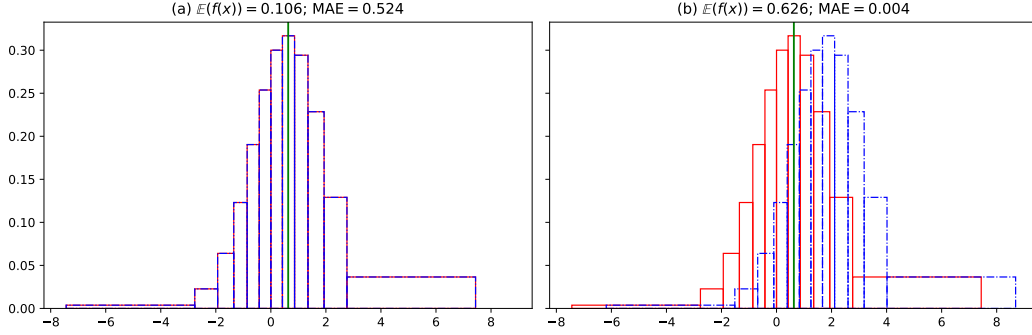


Figure 6: For each figure, the two output histograms are displayed in red and blue. The ground-truth value is displayed by the green line. (a) shows a multi-histogram scenario with normal bin distributions where the two output histograms share the bin endpoint. (b) shows a multi-histogram scenario where the two output histograms’ bin endpoint distributions are adjusted using eq. (13).

bin endpoints. Similarly, fig. 6 (b) shows an example of this for normally distributed bin endpoints. For both examples, the MAE between the expected value of the histogram and the ground-truth value is shown. We see that in both cases, simply shifting the bin distribution for the second histogram massively reduces this MAE.

To expand our algorithm to support multiple bin endpoints, we begin with the single endpoint scenario. We then slightly offset the  $i^{\text{th}}$  histogram’s bin endpoints by  $\frac{i}{M}\mathbb{E}(w)$ , where  $M$  is the number of histograms in our output head. Concretely, for multiple histograms, we let  $\vec{b}_0$  be the bin distribution as defined in eq. (4):

$$\vec{b}_0 = [0 + \epsilon, Q_B(0), Q_B(1/N), Q_B(2/N), \dots, Q_B(1 - 1/N), 1 - \epsilon] \quad (12)$$

Then, the  $i^{\text{th}}$  histogram’s bin endpoints,  $\vec{b}_i$ , is given by:

$$\vec{b}_i = \vec{b}_0 + \frac{i}{M}\mathbb{E}(w) \quad (13)$$

## A.5 Proofs for Loss Gradient Norm Bounds

### A.5.1 Distributional Loss Function

The proof for lemma 1 is very similar to the proof found in Appendix A of Imani and White [15].

**Lemma 1.** *The gradient norm of the histogram loss term of DMoE is bounded as follows:*

$$\left\| \frac{\partial}{\partial \theta} [\vec{p} \cdot \log f(x)] \right\| \leq \|f(x) - \vec{p}\| \cdot \left\| \frac{\partial g(x)}{\partial \theta} \right\| \quad (14)$$

where  $\frac{\partial g(x)}{\partial \theta}$  denotes the Jacobian of the model,  $g(x)$ .

*Proof.* We begin by taking the gradient using the chain rule.

$$\begin{aligned}
\frac{\partial}{\partial \theta} [\vec{p} \cdot \log f(x)] &= \frac{\partial g(x)}{\partial \theta} \frac{\partial f(x)}{\partial g(x)} \left[ \vec{p} \cdot \frac{1}{f(x)} \right] \\
\left( \frac{\partial f(x)}{\partial g(x)} \left[ \vec{p} \cdot \frac{1}{f(x)} \right] \right)_i &= \sum_j p_j \frac{1}{f_j(x)} f_j(x) (1_{i=j} - f_i(x)) \\
&= \sum_j p_j (1_{i=j} - f_i(x)) \\
&= p_i - f_i(x) \sum_j p_j \\
&= p_i - f_i(x)
\end{aligned}$$

We put this term back into the main equation and take the norm.

$$\begin{aligned}
\frac{\partial}{\partial \theta} [\vec{p} \cdot \log f(x)] &= \frac{\partial g(x)}{\partial \theta} [\vec{p} - f(x)] \\
\left\| \frac{\partial}{\partial \theta} [\vec{p} \cdot \log f(x)] \right\| &\leq \|\vec{p} - f(x)\| \left\| \frac{\partial g(x)}{\partial \theta} \right\|
\end{aligned}$$

□

### A.5.2 Distance-based Loss Function

**Lemma 2.** *The gradient norm of the distance-based loss term of DMoE is bounded as follows:*

$$\left\| \frac{\partial}{\partial \theta} \left| \vec{p} \cdot \vec{b} - f(x) \cdot \vec{b} \right| \right\| \leq \sqrt{2} \|f(x)\|_2 \cdot \|\vec{b}\| \cdot \|f(x) - \vec{p}\| \cdot \left\| \frac{\partial g(x)}{\partial \theta} \right\| \quad (15)$$

where  $\frac{\partial g(x)}{\partial \theta}$  denotes the Jacobian of the model,  $g(x)$ .

*Proof.* We begin by taking the gradient using the chain rule.

$$\begin{aligned}
\frac{\partial}{\partial \theta} \left| \vec{p} \cdot \vec{b} - f(x) \cdot \vec{b} \right| &= \frac{\partial g(x)}{\partial \theta} \frac{\partial f(x)}{\partial g(x)} \left[ \frac{\partial \ell_1}{\partial f(x)} \left( \vec{p} \cdot \vec{b} - f(x) \cdot \vec{b} \right) \right] \\
\text{where } \left( \frac{\partial \ell_1}{\partial f(x)} \right)_i &= \begin{cases} +1, & f(x)_i > \vec{p}_i \\ -1, & f(x)_i < \vec{p}_i \end{cases}
\end{aligned}$$

We then take the norm of the gradient.

$$\begin{aligned}
\left\| \frac{\partial}{\partial \theta} \left| \vec{p} \cdot \vec{b} - f(x) \cdot \vec{b} \right| \right\| &= \left\| \frac{\partial g(x)}{\partial \theta} \frac{\partial f(x)}{\partial g(x)} \frac{\partial \ell_1}{\partial f(x)} \left( \vec{p} \cdot \vec{b} - f(x) \cdot \vec{b} \right) \right\| \\
&\leq \left\| \frac{\partial g(x)}{\partial \theta} \right\| \left\| \frac{\partial f(x)}{\partial g(x)} \right\| \left\| \vec{p} \cdot \vec{b} - f(x) \cdot \vec{b} \right\|
\end{aligned}$$

Now,  $\left\| \frac{\partial f(x)}{\partial g(x)} \right\|$  is the norm of the gradient of our softmax output head. We bound this

norm.

$$\begin{aligned}
\left\| \frac{\partial f(x)}{\partial g(x)} \right\| &\leq \left[ \sum_i \sum_j \left| \frac{\partial f_i(x)}{\partial g_j(x)} \right|^2 \right]^{\frac{1}{2}} \\
\sum_i \sum_j \left| \frac{\partial f_i(x)}{\partial g_j(x)} \right|^2 &= \sum_i \sum_j |f_j(x) (1_{i=j} - f_i(x))|^2 \\
&= \left[ \sum_i |f_i(x) \cdot (1 - f_i(x))|^2 \right] \quad \text{when } (i = j) \\
&\quad + \left[ \sum_i \sum_j |-f_i(x) f_j(x)|^2 \right] \quad \text{when } (i = j) \text{ or } (i \neq j) \\
&\quad - \left[ \sum_i |-f_i(x) f_i(x)|^2 \right] \quad \text{when } (i = j)
\end{aligned}$$

We begin by taking the first term:  $\sum_i |f_i(x) \cdot (1 - f_i(x))|^2$ .

$$\begin{aligned}
\sum_i |f_i(x) \cdot (1 - f_i(x))|^2 &= \sum_i |f_i(x) - f_i^2(x)|^2 \\
&= \sum_i (f_i(x) - f_i^2(x))^2 \\
&= \sum_i f_i^2(x) (f_i(x) - 1)^2 \\
&\leq \sum_i f_i^2(x)
\end{aligned}$$

We then take the second term:  $\sum_i \sum_j |-f_i(x) f_j(x)|^2$ .

$$\begin{aligned}
\sum_i \sum_j (-f_i(x) f_j(x))^2 &= \sum_i \sum_j f_i^2(x) f_j^2(x) \\
&= \left( \sum_i f_i^2(x) \right) \left( \sum_j f_j^2(x) \right) \\
&= \left( \sum_i f_i^2(x) \right)^2 \\
&\leq \sum_i f_i^2(x)
\end{aligned}$$

Finally, we take the third term:  $\sum_i |-f_i(x) f_i(x)|^2$ .

$$\begin{aligned}
\sum_i |-f_i(x) f_i(x)|^2 &= \sum_i (-f_i(x) f_i(x))^2 \\
&= \sum_i (f_i^2(x))^2 \\
&= \sum_i f_i^4(x) \\
&\geq 0
\end{aligned}$$

We sum all these terms.

$$\begin{aligned}
\sum_i \sum_j \left| \frac{\partial f_i(x)}{\partial g_j(x)} \right|^2 &= \left[ \sum_i |f_i(x) \cdot (1 - f_i(x))|^2 \right] \\
&+ \left[ \sum_i \sum_j |-f_i(x) f_j(x)|^2 \right] \\
&- \left[ \sum_i |-f_i(x) f_i(x)|^2 \right] \\
&\leq \left[ \sum_i f_i^2(x) \right] + \left[ \sum_i f_i^2(x) \right] \\
&= 2 \sum_i f_i^2(x)
\end{aligned}$$

We solve for the bound of  $\left\| \frac{\partial f(x)}{\partial g(x)} \right\|$ .

$$\begin{aligned}
\left[ \sum_i \sum_j \left| \frac{\partial f_i(x)}{\partial g_j(x)} \right|^2 \right]^{\frac{1}{2}} &\leq \left[ 2 \sum_i f_i^2(x) \right]^{\frac{1}{2}} \\
&= \sqrt{2} \|f(x)\|_2
\end{aligned}$$

Finally, we evaluate for the final bounds.

$$\begin{aligned}
\left\| \frac{\partial}{\partial \theta} \left[ \vec{p} \cdot \vec{b} - f(x) \cdot \vec{b} \right] \right\| &\leq \left\| \frac{\partial g(x)}{\partial \theta} \right\| \left\| \frac{\partial f(x)}{\partial g(x)} \right\| \left\| \vec{p} \cdot \vec{b} - f(x) \cdot \vec{b} \right\| \\
&\leq \sqrt{2} \|f(x)\|_2 \cdot \left\| \vec{p} \cdot \vec{b} - f(x) \cdot \vec{b} \right\| \cdot \left\| \frac{\partial g(x)}{\partial \theta} \right\| \\
&= \sqrt{2} \|f(x)\|_2 \cdot \left\| \vec{b} \right\| \cdot \left\| \vec{p} - f(x) \right\| \cdot \left\| \frac{\partial g(x)}{\partial \theta} \right\|
\end{aligned}$$

□

### A.5.3 Gradient Norm Theorem

**Theorem 2.** Assume that  $g(x)$  is locally  $l$ -Lipschitz continuous w.r.t the model's parameters,  $\theta$ :

$$\left\| \frac{\partial g(x)}{\partial \theta} \right\| \leq l \tag{16}$$

Then, the norm of the gradient of DMoE loss w.r.t.  $\theta$  is bounded by:

$$\|\nabla_{\theta} L_{DMoE}(f(x), y)\| \leq l \|\vec{p} - f(x)\| \left[ 1 + \sqrt{2} \|f(x)\|_2 \|\vec{b}\| \right] \tag{17}$$

where  $\vec{p}$  is the histogram representation of the target (i.e.,  $\vec{p} = Y = \Phi(y)$ ).

*Proof.* The gradient of the DMoE loss w.r.t.  $\theta$  is:

$$\nabla_{\theta} L_{DMoE}(f(x), y) = \frac{\partial}{\partial \theta} [\vec{p} \cdot \log f(x)] + \frac{\partial}{\partial \theta} \left[ \vec{p} \cdot \vec{b} - f(x) \cdot \vec{b} \right] \tag{18}$$

where the first term is the gradient of the histogram component of the loss w.r.t.  $\theta$  and the second term is the gradient of the distance-based component of the loss w.r.t.  $\theta$ .

For the histogram term, we utilize lemma 1, which provides the following bounds:

$$\left\| \frac{\partial}{\partial \theta} (\vec{p} \cdot \log f(x)) \right\| \leq \left\| \frac{\partial g(x)}{\partial \theta} \right\| \cdot \|\vec{p} - f(x)\|$$

For the distance-based term, we utilize lemma 2, which provides the following bounds:

$$\left\| \frac{\partial}{\partial \theta} |\vec{p} \cdot \vec{b} - f(x) \cdot \vec{b}| \right\| \leq \left\| \frac{\partial g(x)}{\partial \theta} \right\| \cdot \left[ \sqrt{2} \cdot \|f(x)\|_2 \cdot \|\vec{b}\| \cdot \|\vec{p} - f(x)\| \right]$$

Putting the two terms together, we obtain the following bound:

$$\|\nabla_{\theta} L_{DMoE}(f(x), y)\| \leq l \|\vec{p} - f(x)\| \left[ 1 + \sqrt{2} \|f(x)\|_2 \|\vec{b}\| \right] \quad (19)$$

□

## A.6 $\|f^2(x)\|_2$ Values for Different Distributions

Figure 4 shows the  $\|f^2(x)\|_2$  values for the normal, categorical, and uniform distributions.

## A.7 Dataset Histograms

### A.7.1 OC20 Dataset

Figure 7 shows KDE plots for the data distributions of all different splits of the OC20 validation dataset.

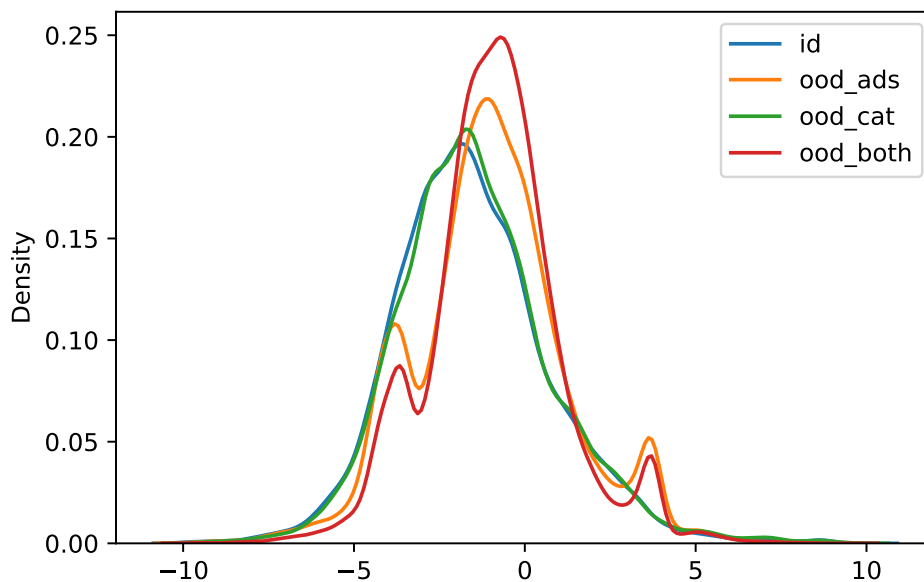


Figure 7: KDE plots for the data distribution of the ID, OOD Ads, OOD Cat, and OOD Both splits of the OC20 validation dataset.

### A.7.2 MD17 Dataset

Figures 8 to 15 show KDE plots for the data distributions of all different molecules in the validation split of the MD17 dataset.

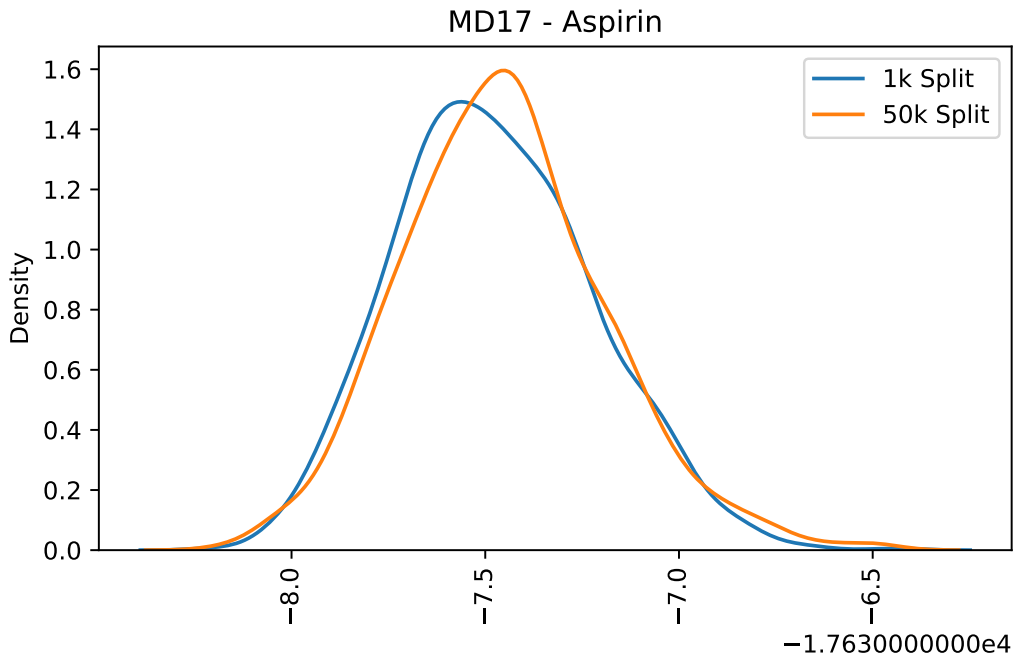


Figure 8: KDE plots for the data distribution of the Aspirin molecule in the MD17 Dataset

### A.7.3 QM9 Dataset

Figures 16 to 27 show KDE plots for the data distributions of all different targets in the validation split of the QM9 dataset.

## A.8 Additional Ablations

### A.8.1 Induced Distribution

Table 15 shows ID validation metrics for training the GemNet+Pos+DMoE model, with different induced distributions, on the OC20 dataset. Specifically, we experiment with Normal, Laplace, Categorical (i.e., one-hot), and K-Categorical (i.e. normalized k-hot) distributions. For the normal distribution, we experiment with different values for  $\sigma$ .

Our results show that the exact details of the choice of induce distribution does not seem to have a huge impact on the accuracy results and much of the differences in performance fall within the margin of error. However, there are some very clear trends that we will analyze below. All these trends are independent of our choice of bin distribution.

The normal distribution (originally suggested by Imani and White [15]) is the optimal choice for the induced distribution. The categorical distribution (referred to as the dirac delta distribution in Imani and White [15]) demonstrates the worst performance. For the normal distribution, lower  $\sigma$  values yield, on average, higher EWT scores but also higher MAE results. Overall, our empirical results demonstrate that using a normal induced distribution with  $\sigma = 1 \cdot \mathbb{E}[w]$  provides a good balance between MAE and EWT results.

### A.8.2 Comparison to Robust Regression Losses

Table 16 shows ID validation metrics for training the GemNet+Pos model on the OC20 dataset, using different loss functions. Specifically, we compare our DMoE (using normal bin distributions) loss with L1 loss, L2 loss, and Smooth L1 Loss [37] (with  $\beta = 1.0$ ). These

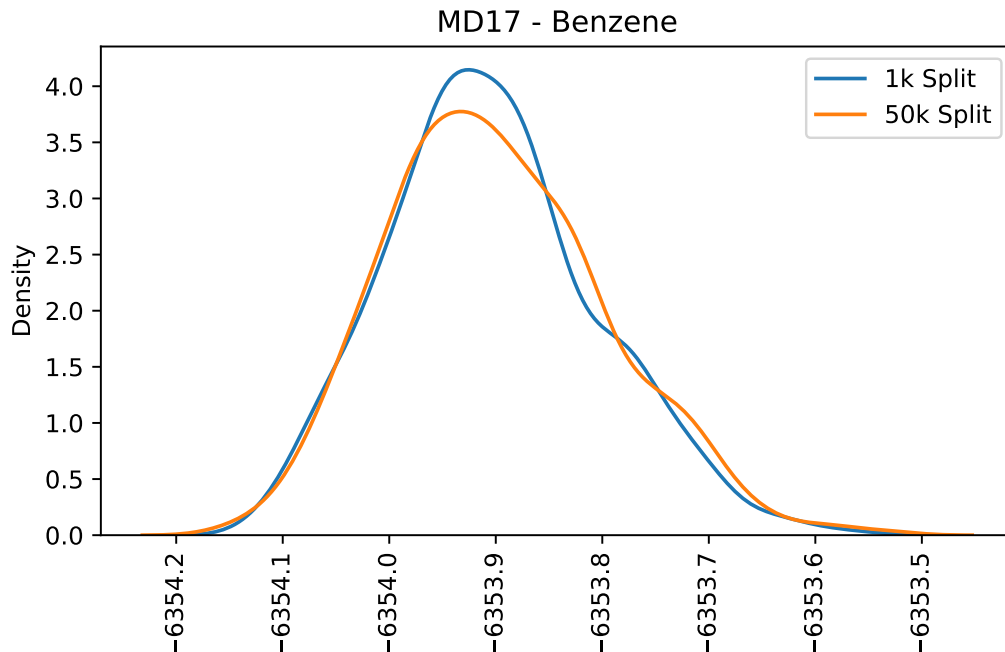


Figure 9: KDE plots for the data distribution of the Benzene molecule in the MD17 Dataset

Table 15: ID Validation metrics for GemNet+Pos+DMoE models trained with different induced distributions on the OC20 dataset

		Normal Bin Distribution		Uniform Bin Distribution	
		Energy MAE	EWT	Energy MAE	EWT
Normal	$\sigma = 0.5 \cdot \mathbb{E}[w]$	0.458	8.0%	0.459	<b>8.0%</b>
	$\sigma = 1 \cdot \mathbb{E}[w]$	0.458	<b>8.1%</b>	0.457	7.9%
	$\sigma = 1.5 \cdot \mathbb{E}[w]$	<b>0.453</b>	7.9%	0.459	7.9%
	$\sigma = 2 \cdot \mathbb{E}[w]$	0.457	7.8%	<b>0.456</b>	<b>8.0%</b>
	$\sigma = 5 \cdot \mathbb{E}[w]$	0.455	7.3%	0.458	7.9%
Laplace	$\sigma = 10 \cdot \mathbb{E}[w]$	0.462	7.0%	<b>0.456</b>	7.6%
K-Categorical	$b = 1 \cdot \mathbb{E}[w]$	0.457	7.7%	0.462	7.9%
Categorical	$k = 3$	0.459	7.8%	0.459	7.8%
		0.460	7.3%	0.463	7.6%

results show that the performance boost that DMoE provides is seemingly different from the effect observed from robust regression losses.

Table 16: ID Validation metrics for GemNet+Pos models trained with different loss functions on the OC20 dataset

	Energy	EwT
L1 Loss	0.476	5.7%
L2 Loss	0.502	4.3%
Smooth L1 Loss	0.505	4.4%
DMoE	<b>0.450</b>	<b>7.8%</b>

## A.9 Optimized Multi-Histogram Implementation

In classic PyTorch code, creating a multi-histogram output head is slow because heads get evaluated sequentially. However, we use FuncTorch [38] to run all these heads in parallel.

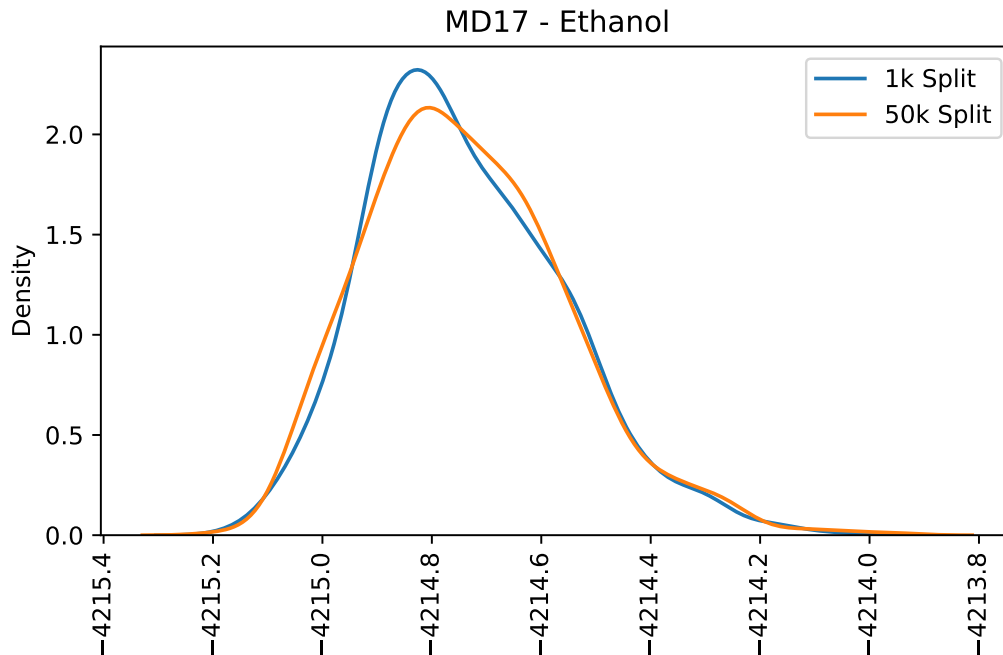


Figure 10: KDE plots for the data distribution of the Ethanol molecule in the MD17 Dataset

An example is shown below.

Let us use the output heads and input shown below.

```
num_histograms = 10
```

```
output_heads = [
    nn.Sequential(
        nn.Linear(input_dim, input_dim // 2),
        nn.ReLU(),
        nn.Linear(input_dim // 2, num_histograms),
    ),
    for _ in range(num_models)
]
```

```
input = torch.randn(1, input_dim)
```

In classic PyTorch, we would use the following sequential code to evaluate all heads:

```
predictions = [output_head(input) for output_head in output_heads]
```

However, with the parallel optimization, we use the following code:

```
fmodel, params, buffers = (
    functorch.combine_state_for_ensemble(output_heads)
)
evaluate_all = functorch.vmap(fmodel, in_dims=(0, 0, None))
predictions = evaluate_all(params, buffers, input)
```



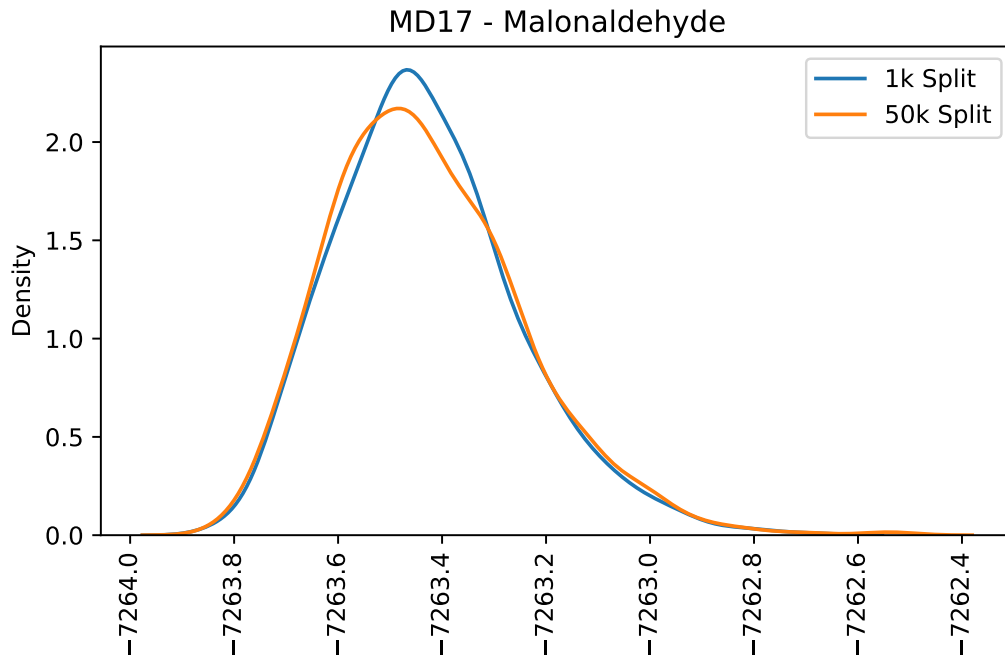


Figure 11: KDE plots for the data distribution of the Malonaldehyde molecule in the MD17 Dataset

## A.10 Model Hyperparameters

In the section below, we enumerate all chosen hyperparameters across all our experiments. Comma-separated hyperparameter values indicate that multiple values were evaluated in our experiments. In this case, an exhaustive grid search is conducted across all possible hyperparameters, and the hyperparameters that produce the best results (i.e., the lowest validation MAE scores) are selected.

For the histogram induced distribution hyperparameter,  $w$  refers to the bin width vector; thus,  $E[w]$  refers to the average bin width in the histogram.

### A.10.1 OC20 Models

Tables 17 to 21 show the hyperparameters for the SchNet, DimeNet++, GemNet-dT, Graphormer, and GemNet\* models, respectively, as shown on tables 1 and 2.

Table 17: SchNet Hyperparameters for OC20 Dataset

Hyperparameter	Value
Number of Hidden Channels	384
Number of Filters to Use	128
Number of Interaction Blocks	4
Number of Gaussians	100
Cutoff Distance for Interatomic Interactions	6
Optimizer	Adam
Learning Rate	0.001
Batch Size	32
Training Time	100 epochs with early stopping
Number of Histograms	1
Number of Histogram Bins	1024
Histogram Bin Distribution	Uniform
Histogram Induced Distribution	Normal( $\sigma = E[w]$ )

Table 18: DimeNet++ Hyperparameters for OC20 Dataset

Hyperparameter	Value
Hidden Embedding Size	256
Embedding Size Used for Atoms in the Output Block	192
Number of Building Blocks	3
Cutoff Distance for Interatomic Interactions	6
Number of Radial Basis Functions	6
Number of Spherical Harmonics	7
Number of Residual Layers in the Interaction Blocks Before the Skip Connection	1
Number of Residual Layers in the Interaction Blocks After the Skip Connection	2
Number of Linear Layers for the Output Blocks	3
Optimizer	Adam
Learning Rate	0.001
Batch Size	12
Training Time	100 epochs with early stopping
Number of Histograms	1
Number of Histogram Bins	1024
Histogram Induced Distribution	Normal( $\sigma = \mathbb{E}[w]$ )

Table 19: GemNet-dT Hyperparameters for OC20 Dataset

Hyperparameter	Value
Number of Radial Basis Functions	128
Number of Spherical Harmonics	7
Number of Building Blocks	3
Number of Output Blocks	4
Embedding Size of the Atoms	512
Embedding Size of the Edges	512
Embedding Size in the Triplet Message Passing Block	64
Embedding Size of the Radial Basis Transformation	16
Embedding Size of the Circular Basis Transformation	16
Edge Embedding Size After the Bilinear Layer	64
Cutoff Distance for Interatomic Interactions	6
Number of Residual Blocks After the Concatenation	1
Number of Residual Blocks in the Atom Embedding Blocks	3
Number of Residual Layers Before Skip	1
Number of Residual Layers After Skip	2
Number of Linear Layers for the Output Blocks	3
Cutoff Distance for Interatomic Interactions	6
Max Number of Neighbors for Interatomic Interactions	50
Auxiliary Position Loss Coefficient	16
Energy Loss Coefficient	1
Optimizer	AdamW
Learning Rate	0.0005
Learning Rate Scheduler	ReduceLRonPlateau
Max Gradient Norm (i.e., Clip Gradient Norm Value)	10
Batch Size	4, 8, 16
Training Time	100 epochs with early stopping
Number of Histograms	1, 8, 32, 256
Number of Histogram Bins	256, 1024, 2048, 4096
Histogram Bin Distribution	Uniform, Normal
Histogram Induced Distribution	Normal( $\sigma = \mathbb{E}[w]$ ), Laplace( $b = \mathbb{E}[w]$ ), Categorical, K-Categorical

Table 20: Graphormer Hyperparameters for OC20 Dataset

Hyperparameter	Value
Number of Radial Basis Functions	128
Number of Building Blocks	12
Number of Building Block Repeats	4
Embedding Size	768
FFN Embedding Size	768
Number of Attention Heads	48
Input Dropout Rate	0
Encoder Layer Dropout Rate	0.1
Attention Dropout Rate	0.1
Activation Dropout Rate	0
Cutoff Distance for Interatomic Interactions	12
Auxiliary Position Loss Coefficient	16
Energy Loss Coefficient	1
Optimizer	Adam
Learning Rate	0.0003
Learning Rate Scheduler	Polynomial decay to 0 over 1 million train steps
Max Gradient Norm (i.e., Clip Gradient Norm Value)	5
Batch Size	2, 4, 6
Training Time	100 epochs with early stopping
Number of Histograms	1, 2, 4
Number of Histogram Bins	256, 1024, 2048, 4096
Histogram Bin Distribution	Uniform, Normal
Histogram Induced Distribution	Normal( $\sigma = \mathbb{E}[w]$ ), Laplace( $b = \mathbb{E}[w]$ ), Categorical, K-Categorical

Table 21: GemNet\* Hyperparameters for OC20 Dataset

Hyperparameter	Value
Number of Radial Basis Functions	128
Number of Spherical Harmonics	7
Number of Building Blocks	12
Number of Building Block Repeats	3
Number of Output Blocks	1
Embedding Size of the Atoms	512
Embedding Size of the Edges	512
Embedding Size in the Triplet Message Passing Block	128
Embedding Size of the Radial Basis Transformation	128
Embedding Size of the Circular Basis Transformation	16
Edge Embedding Size After the Bilinear Layer	128
Cutoff Distance for Interatomic Interactions	12
Number of Residual Blocks After the Concatenation	1
Number of Residual Blocks in the Atom Embedding Blocks	3
Number of Residual Layers Before Skip	1
Number of Residual Layers After Skip	2
Number of Linear Layers for the Output Blocks	3
Cutoff Distance for Interatomic Interactions	6
Max Number of Neighbors for Interatomic Interactions	50
Auxiliary Position Loss Coefficient	16
Energy Loss Coefficient	1
Optimizer	AdamW
Learning Rate	0.0005
Learning Rate Scheduler	ReduceLROnPlateau
Max Gradient Norm (i.e., Clip Gradient Norm Value)	10
Batch Size	1, 2, 4
Training Time	100 epochs with early stopping
Number of Histograms	1, 8, 32, 256
Number of Histogram Bins	256, 1024, 2048, 4096
Histogram Bin Distribution	Uniform, Normal
Histogram Induced Distribution	Normal( $\sigma = \mathbb{E}[w]$ ), Laplace( $b = \mathbb{E}[w]$ ), Categorical, K-Categorical

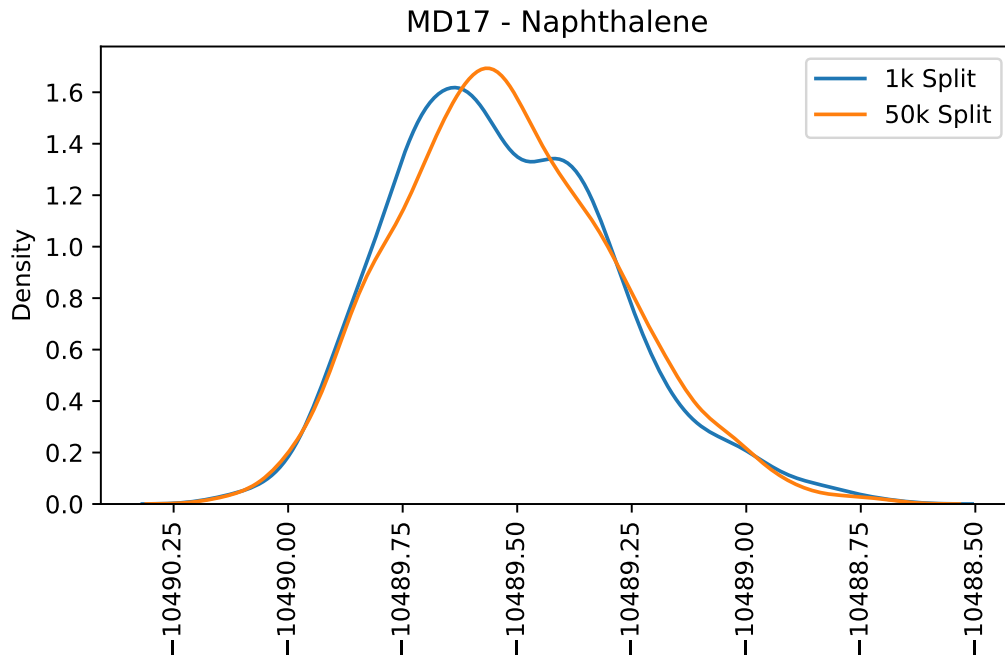


Figure 12: KDE plots for the data distribution of the Naphthalene molecule in the MD17 Dataset

### A.10.2 MD17 Models

Tables 22 and 23 show the hyperparameters for the GemNet-dT and SchNet models, respectively, as shown on table 3.

Table 22: GemNet-dT Hyperparameters for MD17 Dataset

Hyperparameter	Value
Number of Radial Basis Functions	128
Number of Spherical Harmonics	7
Number of Building Blocks	3
Number of Output Blocks	4
Embedding Size of the Atoms	512
Embedding Size of the Edges	512
Embedding Size in the Triplet Message Passing Block	64
Embedding Size of the Radial Basis Transformation	16
Embedding Size of the Circular Basis Transformation	16
Edge Embedding Size After the Bilinear Layer	64
Cutoff Distance for Interatomic Interactions	6
Number of Residual Blocks After the Concatenation	1
Number of Residual Blocks in the Atom Embedding Blocks	3
Number of Residual Layers Before Skip	1
Number of Residual Layers After Skip	2
Number of Linear Layers for the Output Blocks	3
Cutoff Distance for Interatomic Interactions	6
Max Number of Neighbors for Interatomic Interactions	50
Auxiliary Position Loss Coefficient	16
Energy Loss Coefficient	1
Optimizer	AdamW
Learning Rate	0.001, 0.0005, 0.0001
Learning Rate Scheduler	ReduceLROnPlateau
Max Gradient Norm (i.e., Clip Gradient Norm Value)	10
Batch Size	4
Training Time	100 epochs with early stopping
Number of Histograms X Number of Histogram Bins	128x1024, 256x128, 128x64, 2x64
Histogram Bin Distribution	Uniform, Normal
Histogram Induced Distribution	Normal( $\sigma = \mathbb{E}[w]$ )

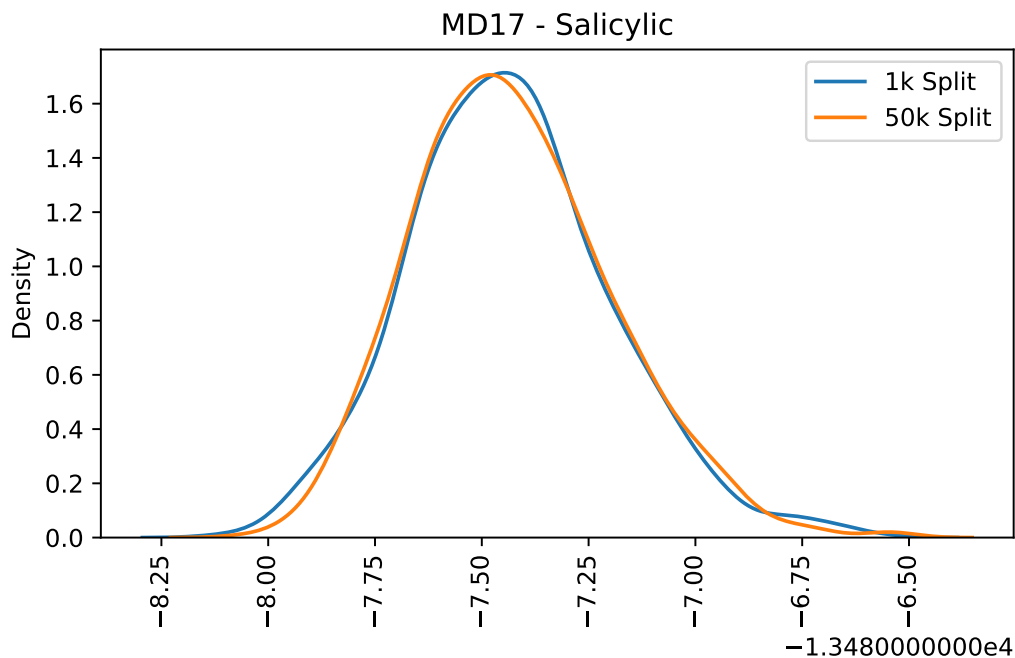


Figure 13: KDE plots for the data distribution of the Salicylic molecule in the MD17 Dataset

Table 23: SchNet Hyperparameters for MD17 Dataset

Hyperparameter	Value
Number of Hidden Channels	384
Number of Filters to Use	128
Number of Interaction Blocks	4
Number of Gaussians	100
Cutoff Distance for Interatomic Interactions	6
Optimizer	Adam
Learning Rate	0.001, 0.0001
Batch Size	4
Training Time	100 epochs with early stopping
Number of Histograms	256
Number of Histogram Bins	256
Histogram Bin Distribution	Normal
Histogram Induced Distribution	Normal( $\sigma = \mathbb{E}[w]$ )

### A.10.3 QM9 Models

Table 24 shows the hyperparameters for the MXMNet model, as shown on table 4.

Table 24: MXMNet Hyperparameters for QM9 Dataset

Hyperparameter	Value
Hidden Dimension Size	128
Number of Hidden Layers	6
Cutoff Distance for Interatomic Interactions for Global Block	5
Optimizer	Adam
Learning Rate	0.0001
Batch Size	128
Training Time	100 epochs with early stopping
Number of Histograms	32
Number of Histogram Bins	2048
Histogram Bin Distribution	Normal
Histogram Induced Distribution	Normal( $\sigma = \mathbb{E}[w]$ )

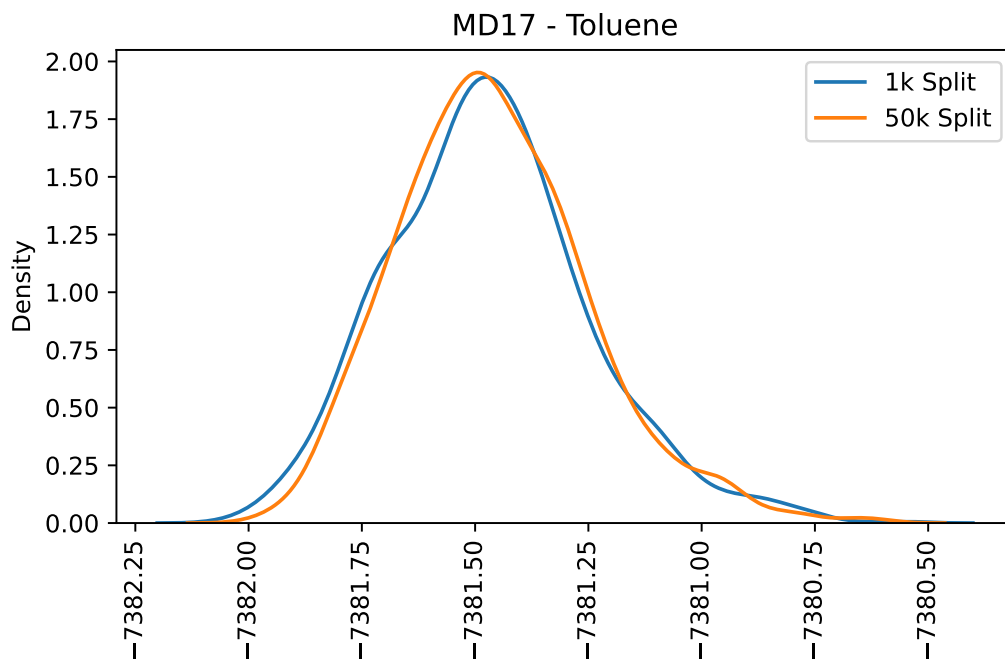


Figure 14: KDE plots for the data distribution of the Toluene molecule in the MD17 Dataset

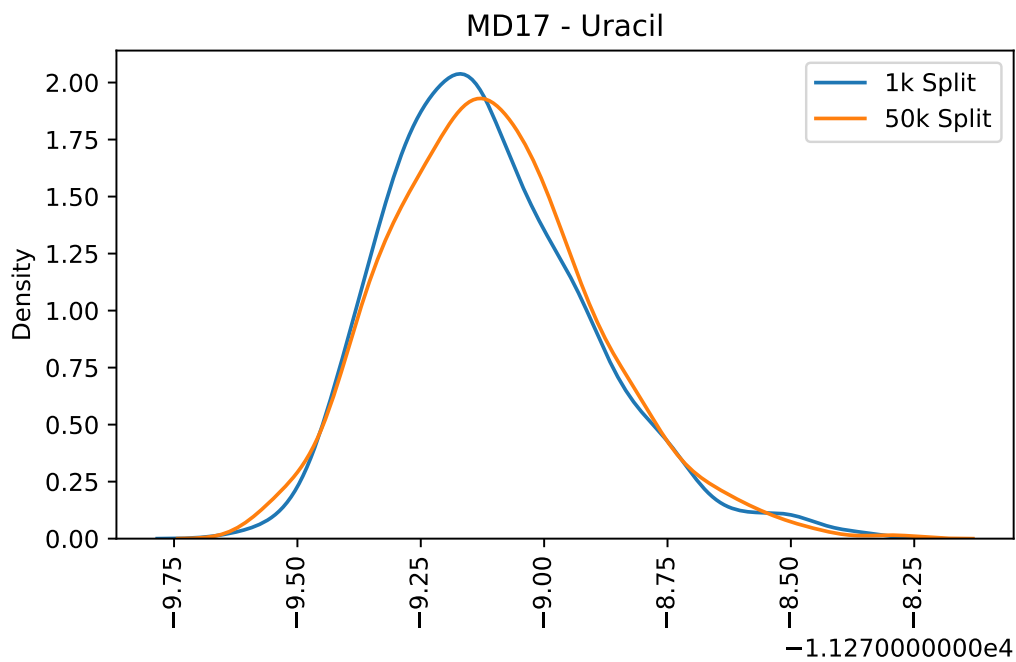


Figure 15: KDE plots for the data distribution of the Uracil molecule in the MD17 Dataset

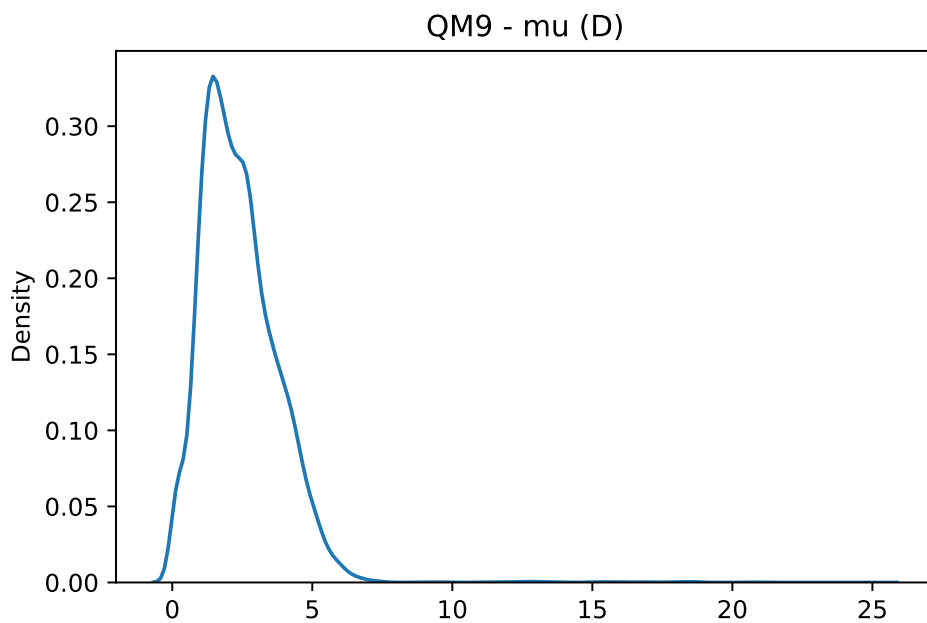


Figure 16: KDE plots for the data distribution of the  $\mu(D)$  target in the QM9 Dataset

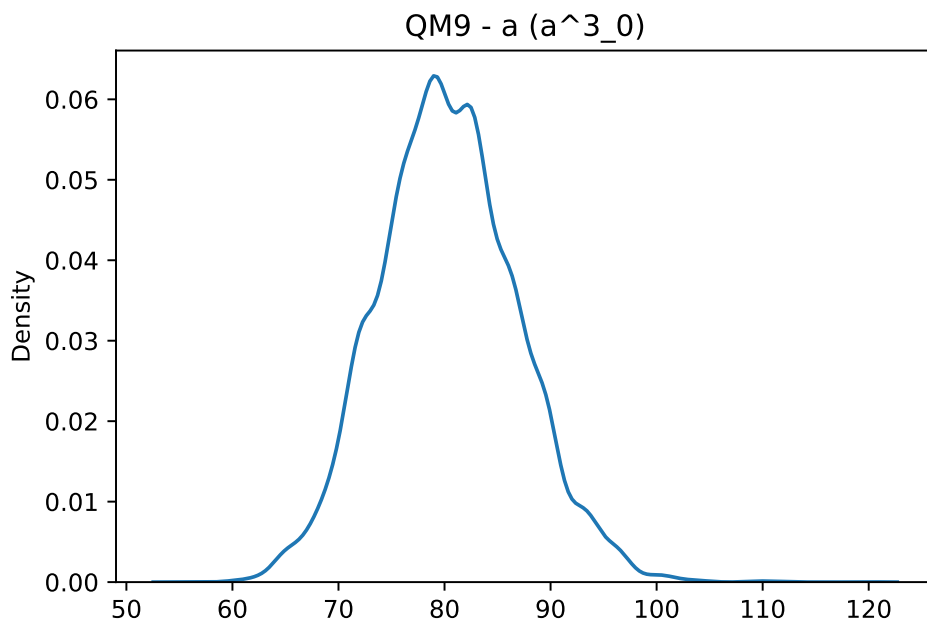


Figure 17: KDE plots for the data distribution of the  $a(a_0^3)$  target in the QM9 Dataset

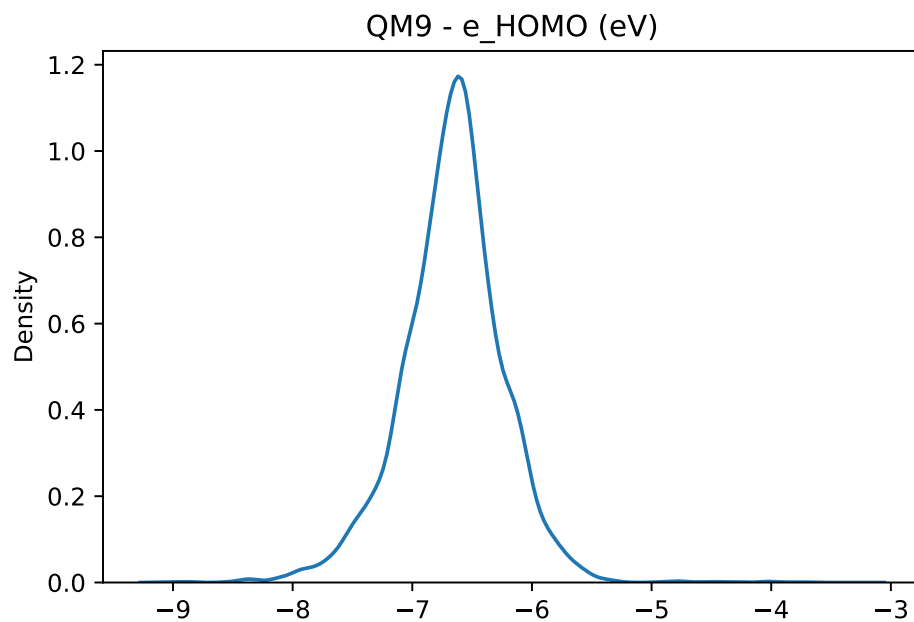


Figure 18: KDE plots for the data distribution of the  $e_{HOMO}$  (eV) target in the QM9 Dataset

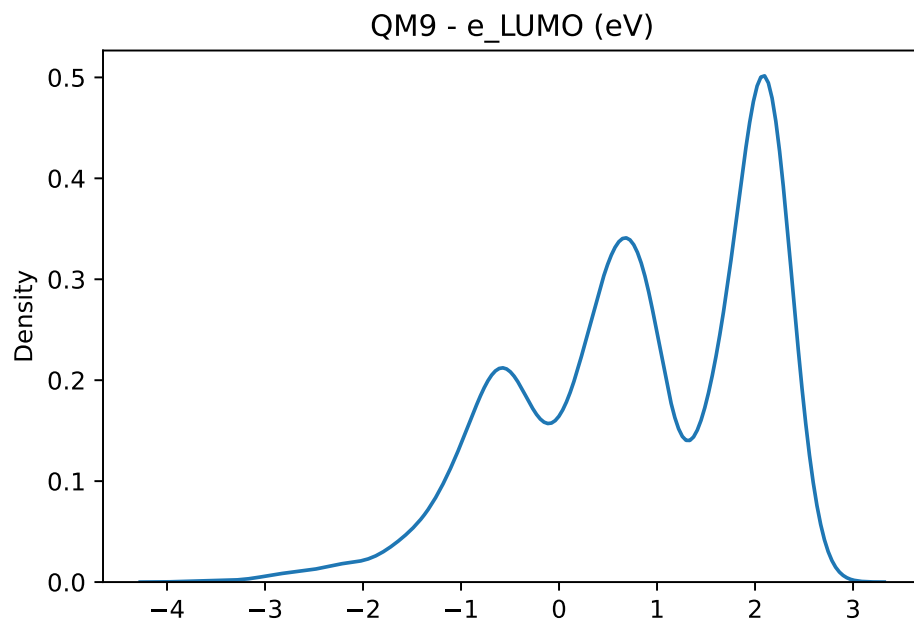


Figure 19: KDE plots for the data distribution of the  $e_{LUMO}$  (eV) target in the QM9 Dataset



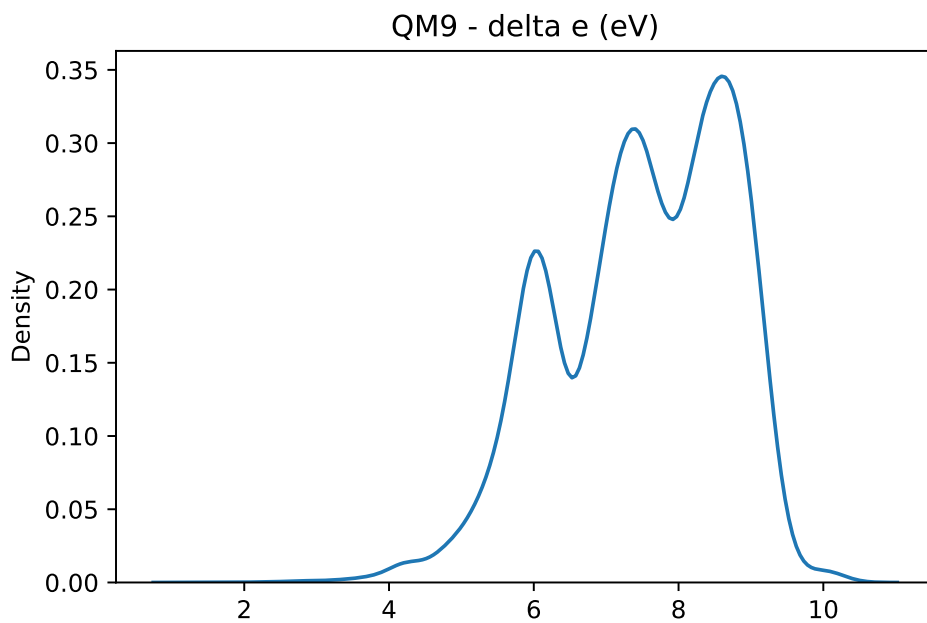


Figure 20: KDE plots for the data distribution of the  $\Delta e$  (eV) target in the QM9 Dataset

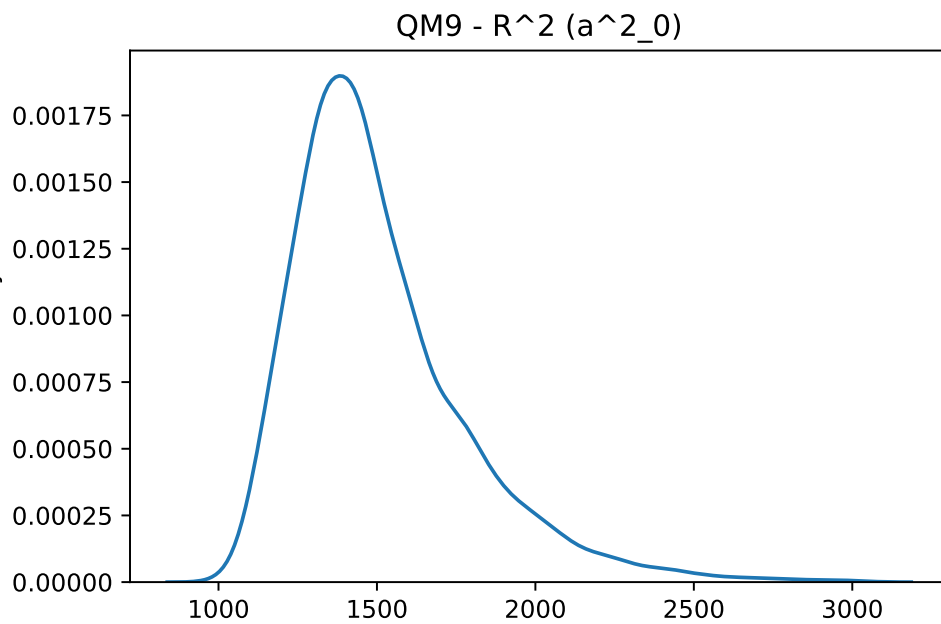


Figure 21: KDE plots for the data distribution of the  $R^2$  ( $a_0^2$ ) target in the QM9 Dataset

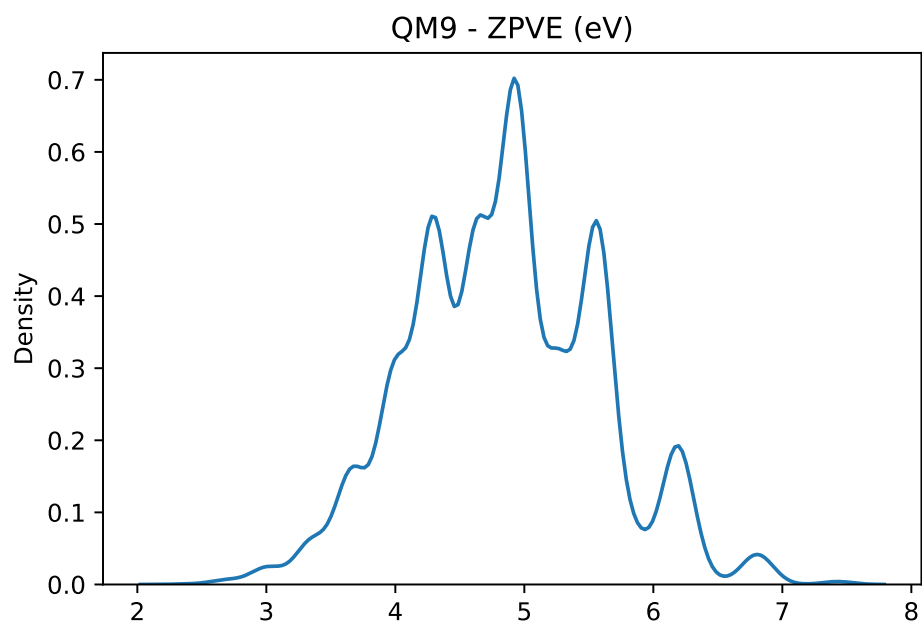


Figure 22: KDE plots for the data distribution of the  $ZPVE$  (eV) target in the QM9 Dataset

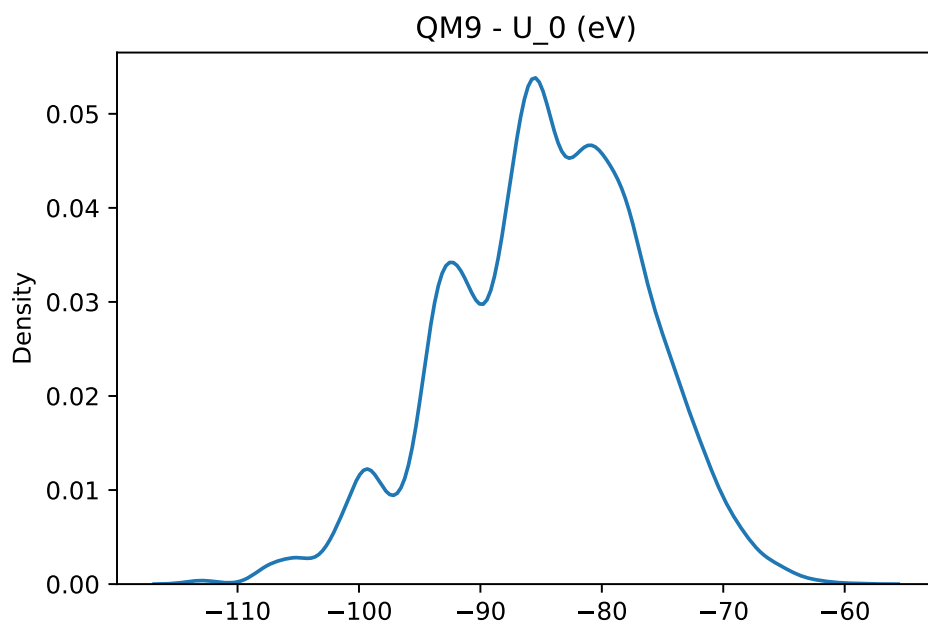


Figure 23: KDE plots for the data distribution of the  $U_0$  (eV) target in the QM9 Dataset

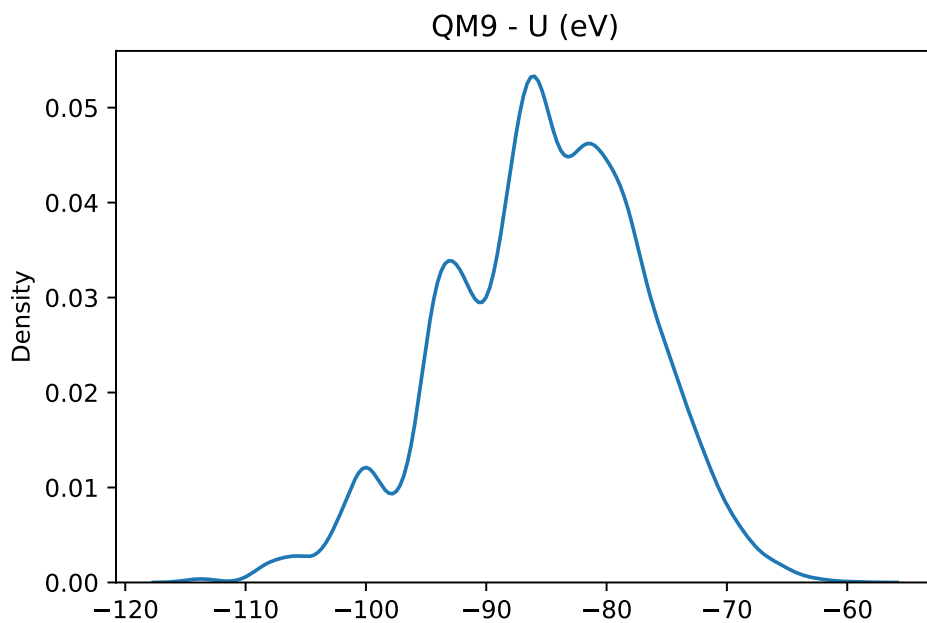


Figure 24: KDE plots for the data distribution of the  $U$  (eV) target in the QM9 Dataset

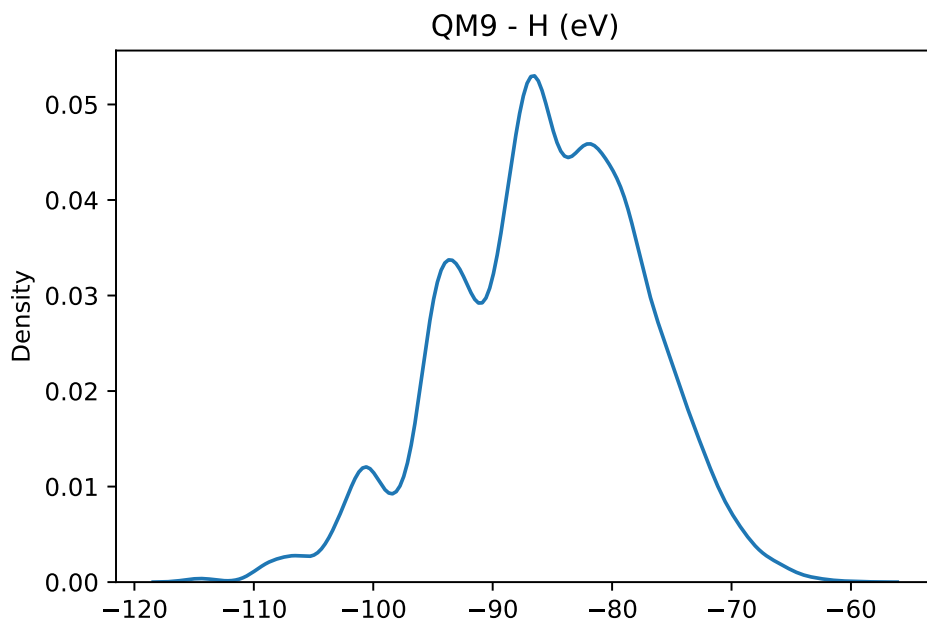


Figure 25: KDE plots for the data distribution of the  $H$  (eV) target in the QM9 Dataset

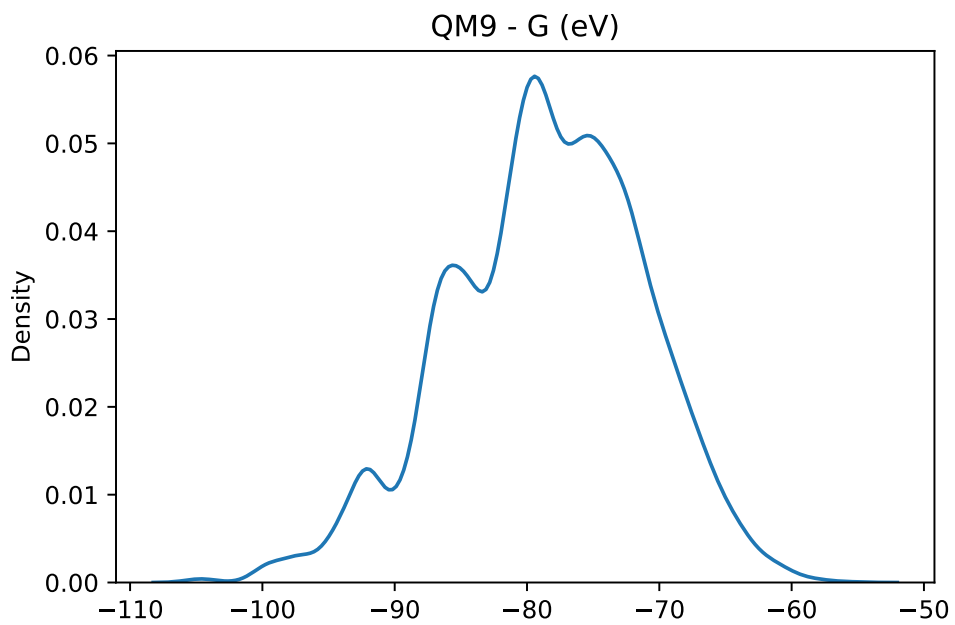


Figure 26: KDE plots for the data distribution of the  $G$  (eV) target in the QM9 Dataset

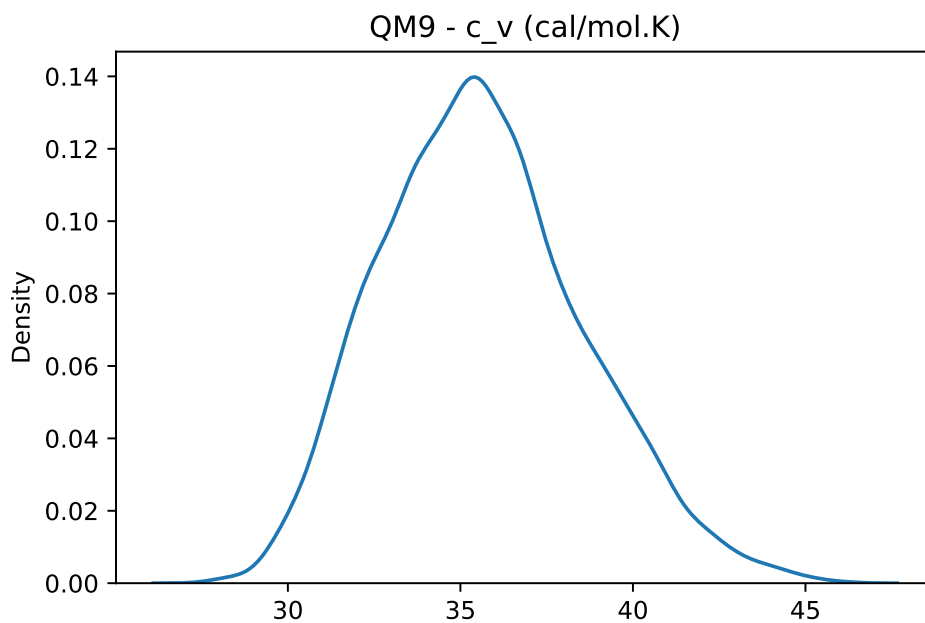


Figure 27: KDE plots for the data distribution of the  $c_v$  (cal/mol.K) target in the QM9 Dataset

## Appendix References

- [1] Simon Batzner, Tess E Smidt, Lixin Sun, Jonathan P Mailoa, Mordechai Kornbluth, Nicola Molinari, and Boris Kozinsky. Se (3)-equivariant graph neural networks for data-efficient and accurate interatomic potentials. *arXiv preprint arXiv:2101.03164*, 2021.
- [4] Lowik Chanussot\*, Abhishek Das\*, Siddharth Goyal\*, Thibaut Lavril\*, Muhammed Shuaibi\*, Morgane Riviere, Kevin Tran, Javier Heras-Domingo, Caleb Ho, Weihua Hu, Aini Palizhati, Anuroop Sriram, Brandon Wood, Junwoong Yoon, Devi Parikh, C. Lawrence Zitnick, and Zachary Ulissi. Open catalyst 2020 (oc20) dataset and community challenges. *ACS Catalysis*, 2021. doi: 10.1021/acscatal.0c04525.
- [10] Johannes Gasteiger, Florian Becker, and Stephan Günnemann. GemNet: Universal directional graph neural networks for molecules. *arXiv preprint arXiv:2106.08903*, 2021.
- [37] Ross Girshick. Fast r-cnn. In *Proceedings of the IEEE international conference on computer vision*, pages 1440–1448, 2015.
- [38] Richard Zou Horace He. functorch: Jax-like composable function transforms for pytorch. <https://github.com/pytorch/functorch>, 2021.
- [15] Ehsan Imani and Martha White. Improving regression performance with distributional losses. In *International Conference on Machine Learning*, pages 2157–2166. PMLR, 2018.
- [40] Adam Paszke, Sam Gross, Francisco Massa, Adam Lerer, James Bradbury, Gregory Chanan, Trevor Killeen, Zeming Lin, Natalia Gimelshein, Luca Antiga, Alban Desmaison, Andreas Kopf, Edward Yang, Zachary DeVito, Martin Raison, Alykhan Tejani, Sasank Chilamkurthy, Benoit Steiner, Lu Fang, Junjie Bai, and Soumith Chintala. Pytorch: An imperative style, high-performance deep learning library. In H. Wallach, H. Larochelle, A. Beygelzimer, F. d'Alché-Buc, E. Fox, and R. Garnett, editors, *Advances in Neural Information Processing Systems 32*, pages 8024–8035. Curran Associates, Inc., 2019. URL <http://papers.neurips.cc/paper/9015-pytorch-an-imperative-style-high-performance-deep-learning-library.pdf>.
- [24] Kristof Schütt, Oliver Unke, and Michael Gastegger. Equivariant message passing for the prediction of tensorial properties and molecular spectra. In *International Conference on Machine Learning*, pages 9377–9388. PMLR, 2021.
- [30] Chengxuan Ying, Tianle Cai, Shengjie Luo, Shuxin Zheng, Guolin Ke, Di He, Yanming Shen, and Tie-Yan Liu. Do transformers really perform badly for graph representation? *Advances in Neural Information Processing Systems*, 34, 2021.